nature portfolio

https://doi.org/10.1038/s41929-021-00668-0

Supplementary information

Enhancing oxygen reduction electrocatalysis by tuning interfacial hydrogen bonds

In the format provided by the authors and unedited

Supplementary Information for

Enhancing Oxygen Reduction Electrocatalysis by Tuning Interfacial Hydrogen Bonds

Tao Wang[1,4,5†], Yirui Zhang[1,2†], Botao Huang[1,4], Bin Cai[1,2], Reshma R. Rao[1,4], Livia Giordano[1,2], Shi-Gang Sun[5], Yang Shao-Horn[1,2,3,4]*

[1]Electrochemical Energy Laboratory Massachusetts Institute of Technology Cambridge, MA 02139, USA

[2]Department of Mechanical Engineering Massachusetts Institute of Technology Cambridge, MA 02139, USA

[3]Department of Materials Science and Engineering Massachusetts Institute of Technology Cambridge, MA 02139, USA

[4]Research Laboratory of Electronics Massachusetts Institute of Technology 77 Massachusetts Avenue, Cambridge, MA 02139, US

[5]Collaborative Innovation Center of Chemistry for Energy Materials, State Key Laboratory for Physical Chemistry of Solid Surfaces, College of Chemistry and Chemical Engineering, Xiamen University, Xiamen, 361005, China

[†]These authors contributed equally: Tao Wang, Yirui Zhang

*Correspondence: shaohorn@mit.edu

Supplementary Methods

Determination of ORR kinetic current.

The ORR current was firstly capacitance-corrected by subtracting the background curve recorded under Ar. Potentials were corrected for the ohmic resistance from the high frequency intercept of the real impedance, which was 30-40 ohms in 0.1 M $HClO_4$. To extract the kinetic current, the mass-transport corrected for Pt/C was carried by the common approach by Koutecký–Levich equation:

$$\frac{1}{i_m} = \frac{1}{i_k} + \frac{1}{i_L} \qquad (1)$$

The i_m is the measured current, the i_L is the mass transport current, the i_k is the kinetic current.

Since the mass transport currents of Au/C were unable to be determined in the polarization curves exactly, the Koutecký–Levich plot were adopted to extract the kinetic current. The i_m^{-1} (measured currents at rotation speed (ω) of 2500 rpm, 1600 rpm, 900 rpm and 400rpm, Supplementary Figure 2 were plotted against the $\omega^{-1/2}$, and the inverse of the kinetic current was obtained by extracting the intercept of the fitting line. The relationship is demonstrated by the equation:

$$\frac{1}{i_m} = \frac{1}{i_k} + \frac{1}{B_L \omega^{1/2}} \qquad (2)$$

The B_L is the Levich Constant, reflecting the number of electrons transferred in the reaction. And the ω is the rotating speed of working electrode [1].

Determination of the electrochemical surface area (ESA).

For Au, the net charge formation of AuO or $Au(OH)_2$ (1.34 V_{RHE} -0.92 V_{RHE}) with double layer correction was integrated. The net charge was then divided by 350 $\mu C/cm^2_{Au}$ (for potential window being 1.7 V_{RHE}) [2], to obtain the ESA of Au. For Pt, the net charge formation of hydrogen adsorption region (0.4 V_{RHE} - 0.02V_{RHE}) and desorption region (0.02 V_{RHE} -0.4V_{RHE}) with double layer correction was integrated. Average the net charge from hydrogen adsorption and desorption, which was then divided by 210 $\mu C/cm^2_{Pt}$ to obtain the ESA of Pt.

Determination of the exchange current density of ORR.

To extract the exchange current density (J_0), the plots of kinetic current density against overpotential were fitted to the Butler-Volmer equation [1]:

$$J_{red/ox}^{BV}(\eta) = J_0[\exp\left(\frac{\alpha F}{RT}\eta\right) - \exp\left(-\frac{(1-\alpha)F}{RT}\eta\right)] \qquad (3)$$

with faraday constant F=96485 C mol^{-1}, idea gas constant R=8.314 J mol^{-1} K^{-1} and temperature T=298.15 K. For Au, the overpotential (η) was defined as the experimentally measured potential (E) subtracted by the equilibrium potential (E_{eq}) of 2e^- pathway of oxygen reduction (O_2+2e^-+2H^+=H_2O_2, E_{eq}=0.68V). For Pt, the overpotential (η) was defined as the experimentally measured potential (E) subtracted by the equilibrium potential (E_{eq}) of 4e^- pathway of oxygen reduction (O_2+4e^- +4H^+=2H_2O, E_{eq}=1.23V). The charge transfer coefficient (α) were set free or fitted to different numbers to find the best fitted curves.

Besides, Marcus-Hush-Chidsey (MHC) formalism was adopted to extract the reorganization energy. Bulter-Volmer equation assumes that the electrostatic energy of the transition state of the reaction is an average of that in the reduced and oxidized states, weighted by the charge transfer coefficient, whereas MHC theory considers solvent reorganization prior to iso-energetic electron transfer [1, 3]. Moreover, MHC theory also considers that electrons in the metal electrode occupying different energy levels around the Fermi level may all participate in the reaction, which can be more accurate and predictive for liquid-solid interfaces [3, 4].

$$j_{red/ox}^{MHC}(\eta) = A\int_{-\infty}^{\infty} exp\left(-\frac{(x-\lambda\pm e\eta)^2}{4\lambda k_B T}\right)\frac{dx}{1+exp(x/k_B T)} \qquad (4)$$

where λ is reorganization energy, k_B is Boltzmann constant, T is temperature, η is the overpotential, A is the pre-exponential factor, accounting for the electronic coupling strength and the electronic density of states (DOS) of the electrode, x accounts for the Fermi statistic of electron energies distributed around electrode potential. The first term in the integrand is the classical Marcus rate for the transfer of an electron of energy x relative to the Fermi level, and the second factor is the Fermi-Dirac distribution assuming a uniform DOS.

Calculation of Proton Potentials.

Proton potentials were scanned along the proton axis of the H-bonded species in reduced state and oxidized state using a reported method[5]. H-bonded species were simulated by DFT for individual ionic liquid cations, and with interaction of individual cations with a H-bond from a nearby OH or OOH, in an implicit solvation model (PCM), and 2-Pentanone (dielectric constant=15.5) was used as solvent [6]. Specifically, the position of the transferring H was optimized for the reduced state (with H on O) and the oxidized state (with H on N), when all other atoms remained fixed. The hydrogen positions obtained from these constrained optimizations were used to define the proton axis for each O–N distance by connecting the optimized hydrogen positions for the reduced and oxidized states. The proton potentials were generated on a one-dimensional grid along this axis for each O–N distance. The hydrogen was moved along the axis of H-bond, the step is 0.05Å, and a single point DFT calculation was performed for each hydrogen position to generate the proton potential curve. The B3LYP functional and 6-311++G** basis set were used, as implemented in the Gaussian (g16) suite [7].

Calculation of Proton Wavefunctions and Energy levels.

The proton wavefunctions and their energy levels were calculated for different H-bonded species by solving 1D the one-dimensional Schrödinger equation numerically based on the proton potential obtained in the former part, using the Fourier Grid Hamiltonian Multiconfigurational Self-Consistent-Field (FGH-MCSCF) method developed by the Hammes-Schiffer group [8, 9]. The calculation package was downloaded via webPCET [9].

Calculation of Boltzmann Probability (P_μ) and Integral Overlap of Proton Vibrational Wavefunctions ($S_{\mu,\nu}$).

P_μ and $S_{\mu,\nu}$ of H-bonded species in different states were calculated. μ represent the reactant of ORR (the oxidized states) and ν represent the product of ORR (the reduced states). Specifically, P_μ is calculated from energy level of different vibrational states following the equation:

$$P_\mu = \frac{e^{-\frac{E_\mu}{k_B T}}}{\sum_n e^{-\frac{E_n}{k_B T}}} \qquad (5)$$

E_n is the energy level of different vibrational states, T is 298.15K in this analysis.

Besides, $S_{\mu,\nu}$ is the integral overlap of proton vibrational wavefunctions which is calculated by integrating numerically for the wavefunctions depicted in Supplementary Figure 23 to Supplementary Figure 28.

Estimation of the Rate Constant of PCET reaction. Based on the physical quantities obtained in former part, we could predict the k_0 (rate constant at equilibrium state) of PCET relevant step in ORR ($OOH_{Au} + H^+ + e^- = H_2O_2$ and $OH_{Pt} + H^+ + e^- = H_2O$), following the rate constant expression derived by the Hammes-Schiffer group [5, 10]:

$$k_0 = \sum_{\mu,\nu} P_\mu \frac{(V^{el} S_{\mu,\nu})^2}{\hbar} \sqrt{\frac{\pi}{\lambda k_B T}} \exp\left[-\frac{(\Delta G^0_{\mu,\nu}+\lambda)^2}{4\lambda k_B T}\right] \qquad (6)$$

T is 298.15K in this analysis, and $\Delta G_{\mu,\nu}{}^0$ is the energy difference between states ν and μ, which could be extracted from E_n. The methods for calculating P_μ and $S_{\mu,\nu}$ have been described before. The rate constant is proportional to $P_\mu S_{\mu,\nu}{}^2$ according to the expression depicted here. Besides, V^{el} is the electronic coupling, which depends on the distance between electron donor and acceptor. We assumed the distance between electrode and the ORR intermediate (OOH on Au and OH on Pt) is unchanged in different ionic liquids, so V^{el} is a constant in our analysis. λ is the reorganization energy. According to the fitting results of ORR polarization curves to MHC theory, the reorganization energy is similar for different ionic liquids and all closed to 1eV (Supplementary Figure 13), which is agree with reorganization energy reported for superoxide reduction in organic solvent[11]. Besides, the reorganization energy could be estimated by a dielectric continuum model, which is predominantly determined by the dielectric constant of solvent. The static dielectric constants of ionic liquids with NTf_2 as anion were all in the range of 12-15 in reported works [12, 13], indicating the reorganization energy shouldn't change evidently in different ionic liquids. So, we assumed λ is 1eV for predicting the rate constants, and the cases of λ=0.75eV and 1.25eV were calculated as well to evaluate the influence of variation in reorganization energy (Supplementary Table 11).

Estimation of the pH effect on ORR on Au

The first step of ORR on Au (O_2+e^-+H^+ => OOH) has been suggested to be the decoupled proton and electron transfer step, the electron transfer (ET) (O_2 + e^- => O_2^-) occurs before proton transfer (PT) (O_2^- + H^+ => OOH). According to the kinetics model developed by Koper[14], the kinetic of this step (O_2+e^-+H^+ => OOH) is affected by pH, following the equation:

$$k_1 = \frac{k_{11}k_{12}}{k_{-11}+k_{12}[H^+]^\alpha} \qquad (7)$$

k_1 is apparent rate constant of O_2+e^-+H^+ => OOH, k_{11} is rate constant of ET (O_2 + e^- => O_2^-), k_{12} is rate constant of PT (O_2^- + H^+ => OOH). α is charge transfer coefficient. In order to estimate the pH effect on rate constant of O_2+e^-+H^+ => OOH in ionic liquid, which changes the local pH on Au surface, we calculated the enhancement of k_1 in different ionic liquids and depicted in Supplementary Figure 11.

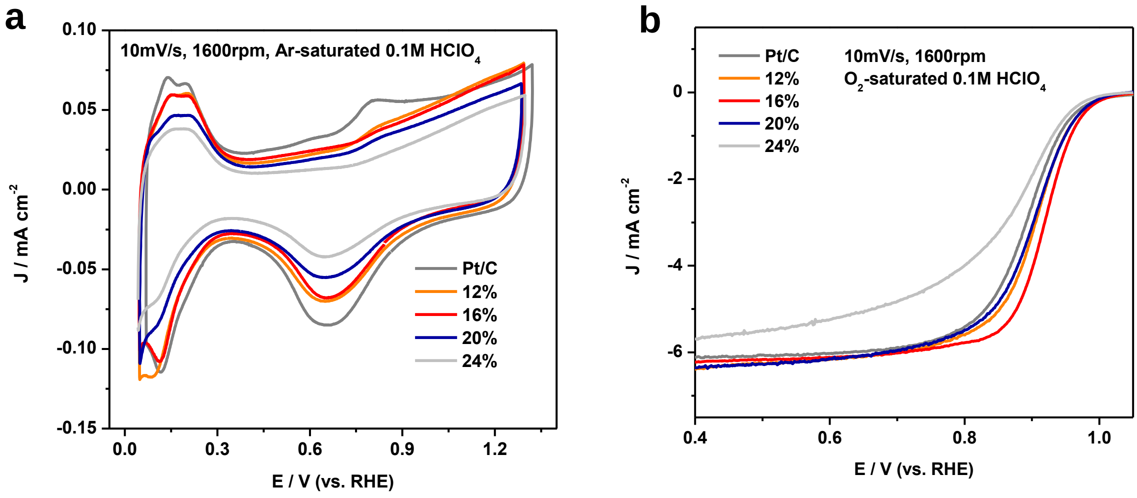

Supplementary Figure 1: IL loading dependent experiments. (a) CV curves of Pt/C modified with different loading of $[C_4C_1im][NTf_2]$ measured in Ar saturated 0.1 M $HClO_4$, rotation speed is 1600 rpm and the scan rate is 10 mV s^{-1}. The counter electrode is Pt wire electrode. The reference electrode is $Hg/HgSO_4$, which was converted to RHE scale by calibrating of HER/HOR polarization test. The average thickness of ionic liquids on Pt/C were estimated to be 0.6 nm for 12% loading, 0.9 nm for 16% loading, 1.1 nm for 20% loading and 1.4 nm for 24% loading, with assumption that the specific surface area of carbon support is 200 $m^2 \cdot g^{-1}$ and the specific surface area of 2nm Pt nanoparticles is 70 $m^2 \cdot g^{-1}$. (b) Background and *iR* corrected ORR polarization curves measured in O_2 saturated 0.1 M $HClO_4$, rotation speed is 1600 rpm, and the scan rate is 10 mV s^{-1}. The loading of Pt was controlled at 20 $\mu g \cdot cm^{-2}$. 0.05 wt% Nafion was added to the catalytic layer. The results suggested 16% is the best loading.

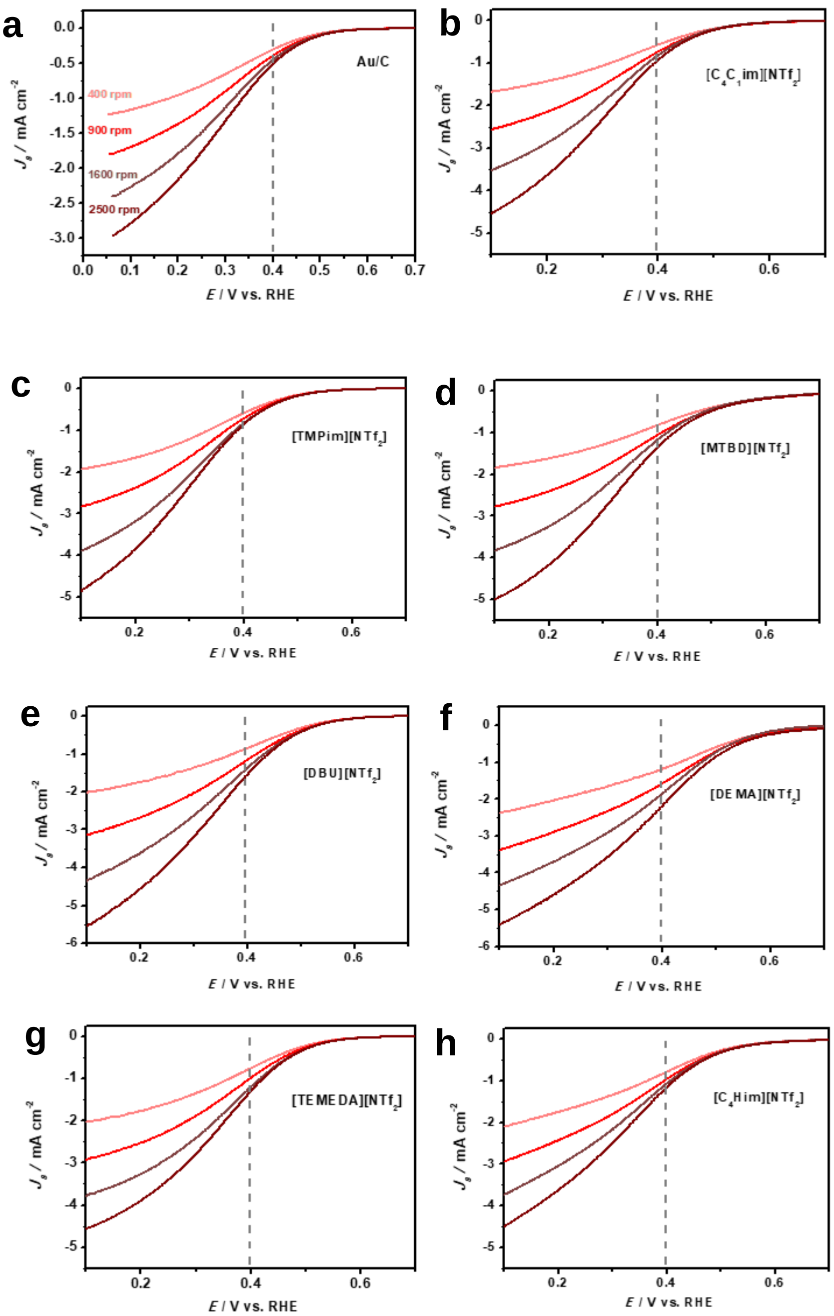

Supplementary Figure 2: Rotation dependent background and *iR* corrected ORR polarization curves of pristine Au/C (a), [C_4C_1im][NTf_2] (b), [TMPim[NTf_2] (c), [MTBD][NTf_2] (d), [DBU][NTf_2] (e), [DEMA][NTf_2] (f), [TEMEDA][NTf_2] (g) and [C_4Him][NTf_2] (h), measured in O_2-saturated 0.1 M $HClO_4$. The rotation speed is controlled at 400 rpm, 900 rpm, 1600 rpm and 2500 rpm, and the scan rate is 10 mV s^{-1}. The counter electrode is graphite electrode. The reference electrode is Hg/$HgSO_4$, which was converted to RHE scale by calibrating of HER/HOR polarization test. The loading of Au was controlled at 40 μg·cm^{-2}, the ionic liquid loading is 16 wt%. 0.05 wt% Nafion was added to the catalytic layer.

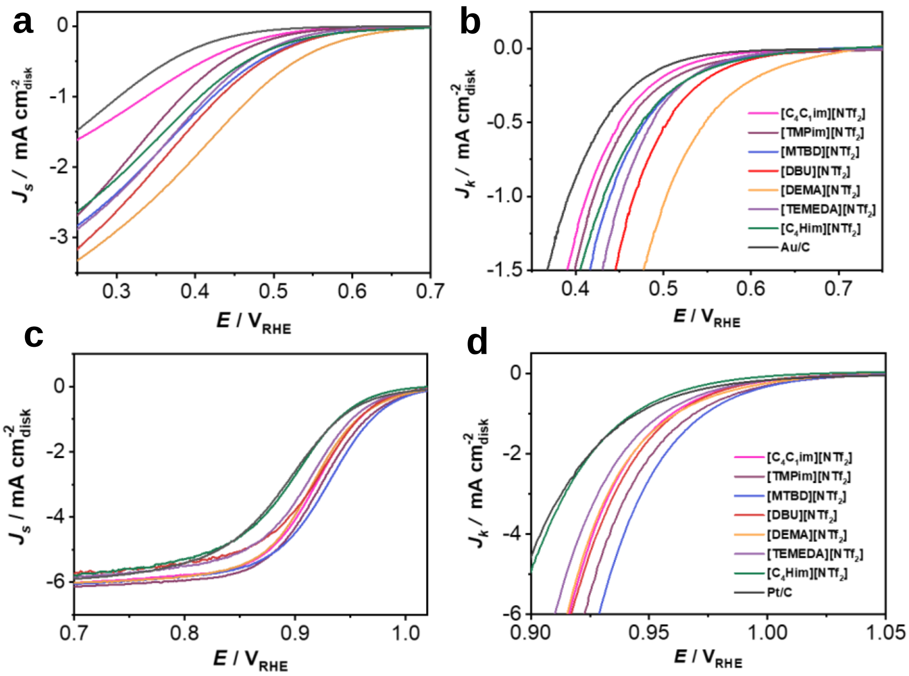

Supplementary Figure 3: (a, c) Background and *iR* corrected ORR polarization curves of ionic-liquid-modified Au/C (a) and Pt/C (c). The polarization curves were measured in O_2-saturated 0.1 M $HClO_4$, with a scan rate of 10 mV/s and the rotation speed is 1600 rpm. The counter electrode is graphite electrode for measurements of Au/C, and is Pt wire electrode for measurements of Pt/C. The reference electrode is Hg/$HgSO_4$, which was converted to RHE scale by calibrating of HER/HOR polarization test. The loading of Au was controlled at 40 μg·cm^{-2} and Pt was controlled at 20 μg·cm^{-2}. 0.05 wt% Nafion was added to the catalytic layer. (b, d) The kinetic currents of Au/C (b) and Pt/C (d) were extracted from polarization curves. Typically, the Koutecký–Levich plot were generated to extract the kinetic currents of Au/C. The inverse of ORR current (i_m^{-1}) measured with 400rpm, 900rpm, 1600rpm and 2500 rpm (Fig. S2) were plot against the $\omega^{-1/2}$, ω is the rotation speed. The inverse of the kinetic current (i_k^{-1}) was obtained by extracting the intercept of the fitting line. Besides, the kinetic currents of Pt/C were extracted by Koutecký–Levich equation directly. The specific method of determination of kinetic current was depicted in Supplementary Methods. The kinetic current densities (J_k) were obtained by normalizing kinetic current (i_k) by the area of working electrode.

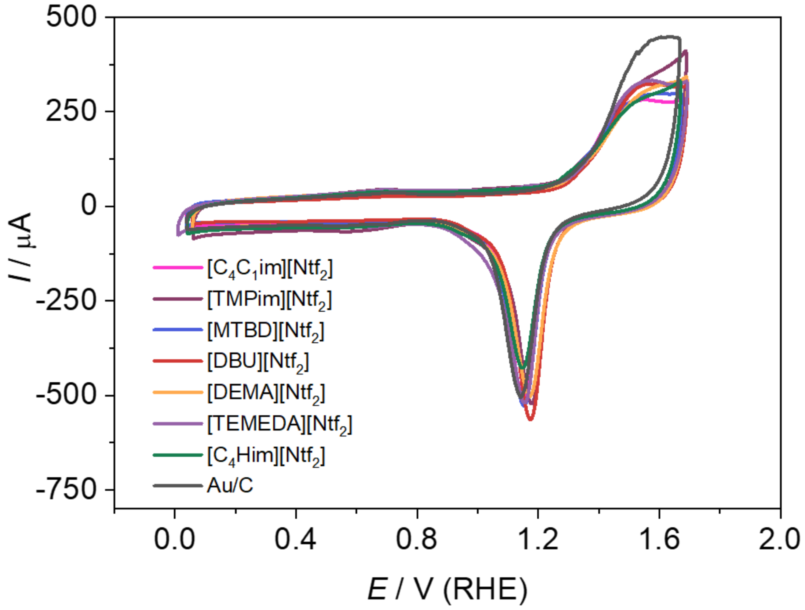

Supplementary Figure 4: CV curves of ionic-liquid-modified Au/C measured in Ar-0.1 M $HClO_4$, rotation speed is 1600 rpm and the scan rate is 50 mV s^{-1}. The counter electrode is graphite electrode. The reference electrode is $Hg/HgSO_4$, which was converted to RHE scale by calibrating of HER/HOR polarization test. The loading of Au was controlled at 40 $\mu g \cdot cm^{-2}$, the ionic liquid loading is 16 wt%. 0.05 wt% Nafion was added to the catalytic layer.

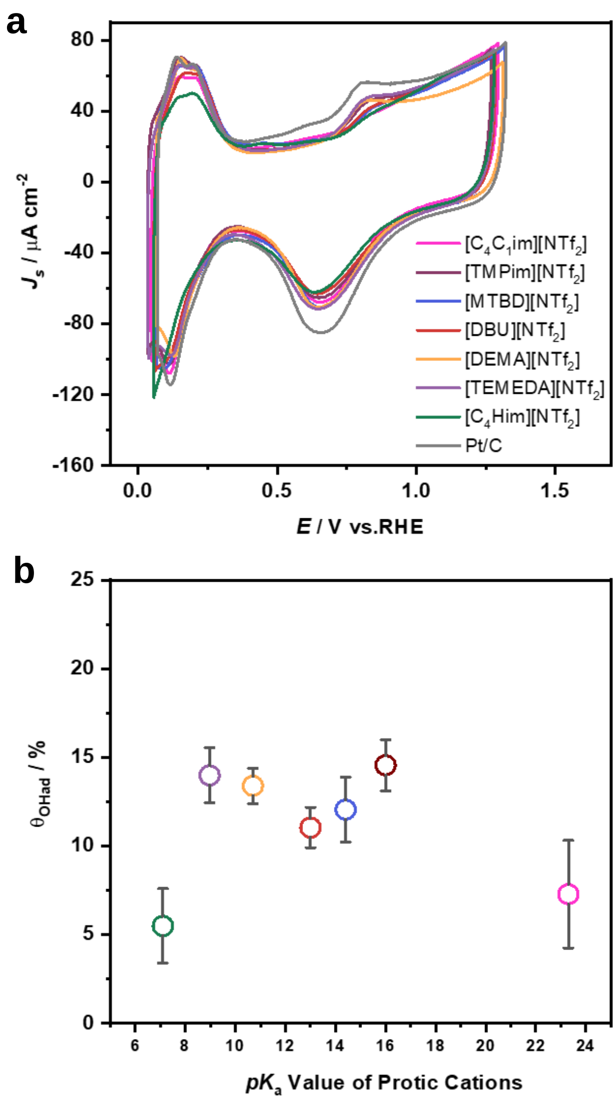

Supplementary Figure 5: (a) CV curves of ionic-liquid-modified Pt/C at 10 mV s^{-1} in Ar-saturated 0.1 M $HClO_4$. The counter electrode is Pt wire electrode. The reference electrode is $Hg/HgSO_4$, which was converted to RHE scale by calibrating of HER/HOR polarization test. The loading of Pt was controlled at 20 μg·cm^{-2}. 0.05 wt% Nafion was added to the catalytic layer. (b) the relationship between OH and O coverage and the pK_a value of cations. Error bars represent standard deviations (SDs) of at least three independent measurements. It should be noted that there are uncertainties in determining OH and O coverage on Pt using CVs, which can be further complicated by inhomogeneous dispersion within the entirety of the catalyst layer and the convolution of double-layer charge associated with OH and O coverage.

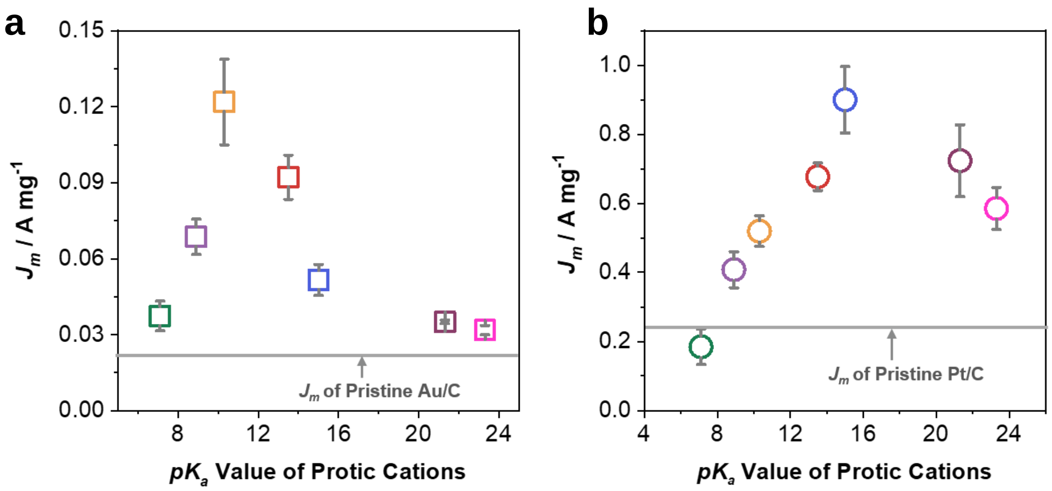

Supplementary Figure 6: The relationship between the mass-normalized kinetic current densities of ionic-liquid-modified Au/C (a), Pt/C (b) as a function of pK_a value of protic cations in ionic liquids. The mass-normalized kinetic current densities were obtained by normalizing kinetic current (i_k) (Supplementary Figure 3) by the mass of Au and Pt deposited on working electrode. Error bars represent SDs of at least three independent measurements.

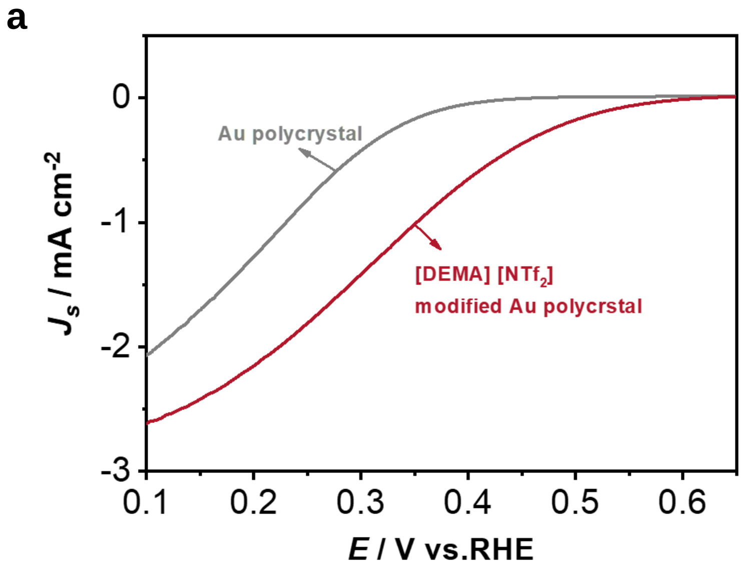

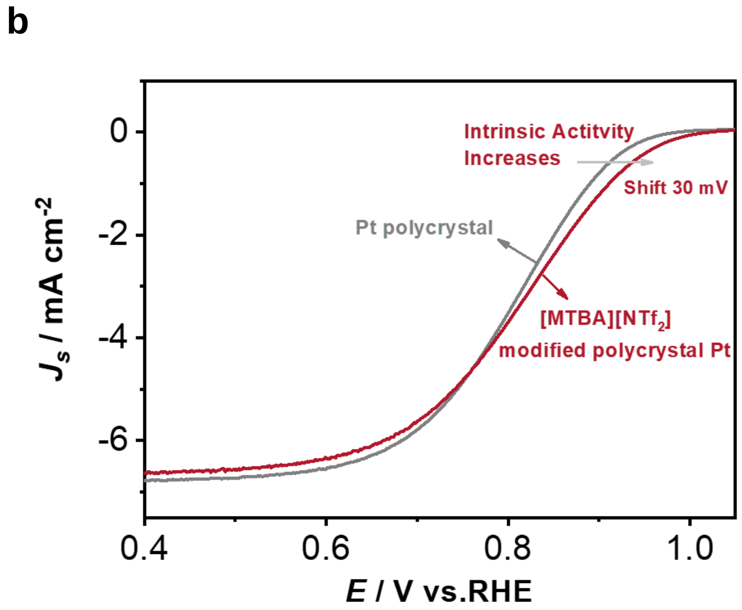

Supplementary Figure 7: Ionic liquid enhancement for bulk electrode. (a) background and *iR*-corrected ORR polarization curves of polycrystal Au electrode and [DEMA][NTf$_2$]-modified polycrystal Au electrode. (b) Background and *iR*-corrected ORR polarization curves of polycrystal Pt electrode and [MTBD][NTf$_2$]-modified polycrystal Pt electrode. The experiments were measured at 10 mV s^{-1} and 1600 rpm in O_2-saturated 0.1 M $HClO_4$. 2μL ionic liquids were deposit on working electrode, resulting in 100 μm ionic liquid layer, which is much thicker than ionic liquid modified nanomaterials.

a

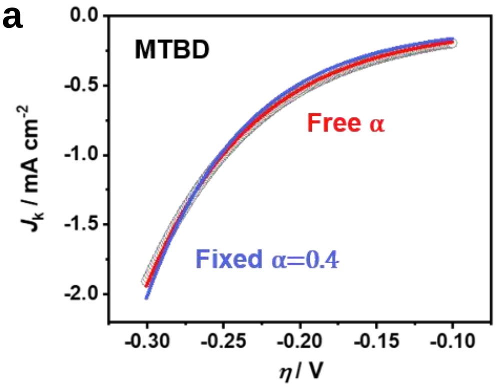

d

α	j_0 / mA cm^{-2}	$j_{0,s}$ / mA cm$_{Au}^{-2}$
0.3626	0.02667	1.46*10^{-3}
0.4	0.01802	9.84*10^{-4}

b

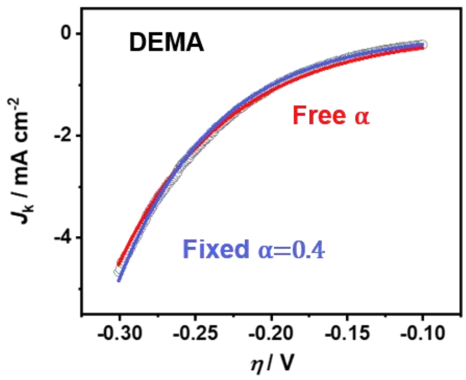

e

α	j_0 / mA cm^{-2}	$j_{0,s}$ / mA cm$_{Au}^{-2}$
0.3563	0.06952	3.38*10^{-3}
0.4	0.04474	2.18*10^{-3}

c

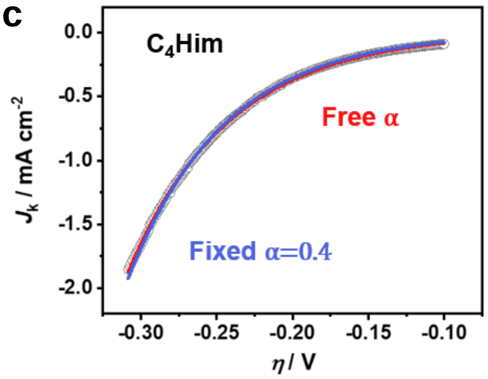

f

α	j_0 / mA cm^{-2}	$j_{0,s}$ / mA cm$_{Au}^{-2}$
0.3848	0.01843	1.09*10^{-3}
0.4	0.01575	9.34*10^{-4}

Supplementary Figure 8: ORR kinetic current density of Au/C modified with [MTBD][NTf$_2$] (a), [DEMA][NTf$_2$] (b) and [C$_4$Him][NTf$_2$] (c) measured in oxygen saturated 0.1M HClO$_4$ (Supplementary Figure 3b) is plotted against overpotential (η) and fitted to the Butler-Volmer equation with faraday constant F=96485 C mol^{-1}, idea gas constant R=8.314 J mol^{-1} K^{-1} and temperature T=293.15K. Charge coefficient α was found in the range of 0.35-0.4 when it free to vary. To simplify comparison, we then fixed α at 0.4 to extract the exchange current density (J_0) of Au/C modified with [MTBD][NTf$_2$] (d), [DEMA][NTf$_2$] (e) and [C$_4$Him][NTf$_2$] (f). The specific exchange current density ($J_{0,s}$) of Au/C modified with [MTBD][NTf$_2$] (d), [DEMA][NTf$_2$] (e) and [C$_4$Him][NTf$_2$] (f) was extracted by normalizing j_0 with electrochemically surface area of Au. The equilibrium potential of ORR on Au was defined as the equilibrium potential of oxygen reducing to H_2O_2 ($O_2 + 2H^+ + 2e^- \rightarrow H_2O_2$, 0.68 V$_{RHE}$).

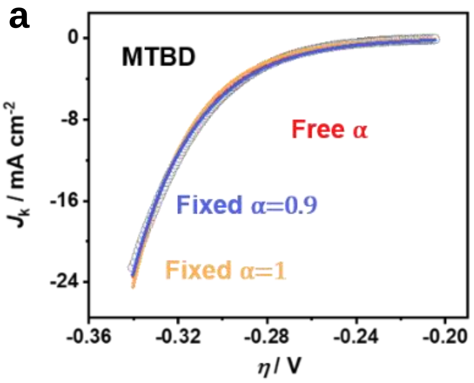

d

α	J_0 / mA cm^{-2}	$J_{0,s}$ / mA cm$_{Pt}^{-2}$
0.9106	1.34*10^{-4}	5.28*10^{-6}
0.9	1.53*10^{-4}	6.02*10^{-6}
1	4.29*10^{-5}	1.68*10^{-6}

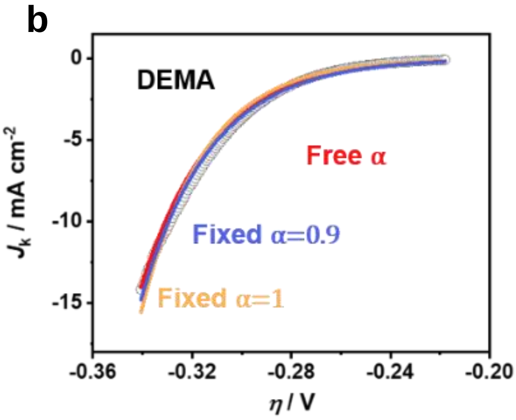

e

α	J_0 / mA cm^{-2}	$J_{0,s}$ / mA cm$_{Pt}^{-2}$
0.8921	1.01*10^{-4}	3.98*10^{-6}
0.9	9.63*10^{-5}	3.79*10^{-6}
1	2.69*10^{-5}	1.06*10^{-6}

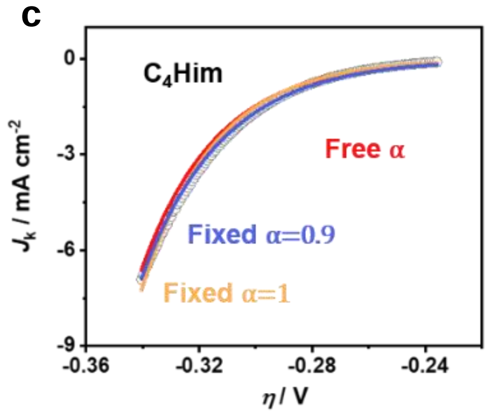

f

α	J_0 / mA cm^{-2}	$J_{0,s}$ / mA cm$_{Pt}^{-2}$
0.9582	2.16*10^{-5}	1.23*10^{-6}
0.9	4.53*10^{-5}	2.59*10^{-6}
1	1.26*10^{-5}	7.20*10^{-7}

Supplementary Figure 9: ORR kinetic current density of Pt/C modified with [MTBD][NTf_2] (a), [DEMA][NTf_2] (b) and [C_4Him][NTf_2] (c) measured in oxygen saturated 0.1M $HClO_4$ (Supplementary Figure 3d) is plotted against overpotential (η) and fitted to the Butler-Volmer equation with faraday constant F=96485 C mol^{-1}, idea gas constant R=8.314 J mol^{-1} K^{-1} and temperature T=293.15K. Charge coefficient α was found in the range of 0.9-1 when it free to vary. To simplify comparison, we then fixed α at 0.9 and 1 to extract the exchange current density (J_0) of Pt/C modified with [MTBD][NTf_2] (e), [DEMA][NTf_2] (d) and [C_4Him][NTf_2] (f). The specific exchange current density ($J_{0,s}$) of Pt/C modified with [MTBD][NTf_2] (e), [DEMA][NTf_2] (d) and [C_4Him][NTf_2] (f). was extracted by normalizing J_0 with electrochemically surface area of Pt. The equilibrium potential of ORR on Pt was defined as the equilibrium potential of oxygen reducing to H_2O ($O_2 + 4H^+ + 4e^- \rightarrow H_2O$, 1.23 V_{RHE}).

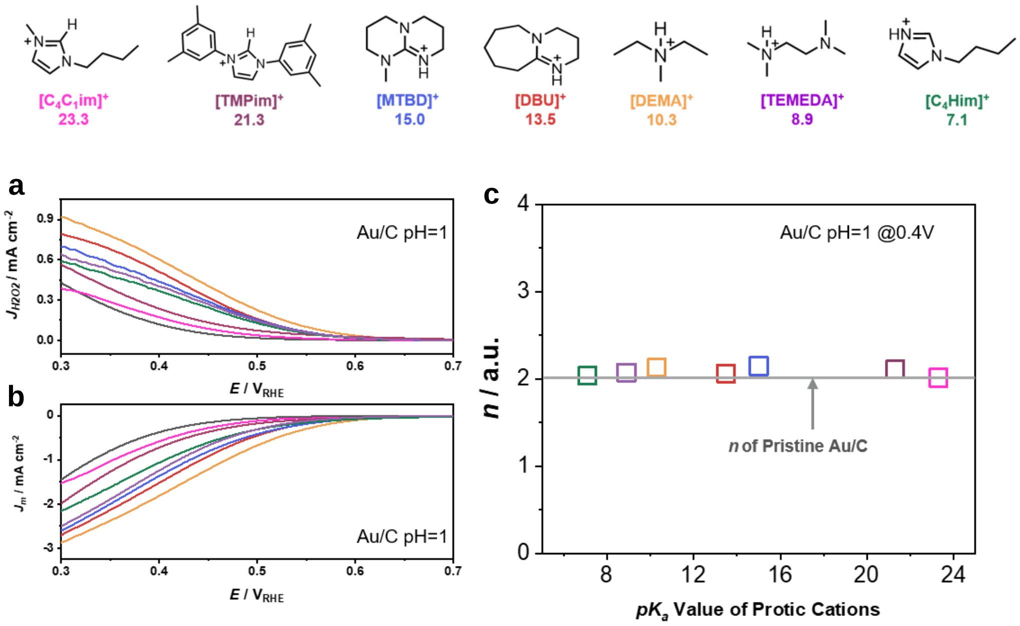

Supplementary Figure 10: pK_a-dependent ORR activity on Au/C measured in O_2-saturated 0.1 M $HClO_4$, with a scan rate of 10 mV/s and the rotation speed is 1600 rpm. (a) The H_2O_2 production in ORR process (denoted as *n*) measured on ionic-liquids-modified Au/C by RRDE; (b) Background and *IR* corrected ORR polarization curves of ionic-liquids-modified Au/C; (c) The number of electrons transferred in ORR process (denoted as *n*) was extracted from J_m and J_{H2O2} following the equation that $n = 4 \times \frac{J_m}{J_m + \frac{J_{H_2O_2}}{N_c}}$ (8), N_c is the collection efficiency of RRDE which is 0.37 here. The loading of Au was controlled at 40 μg·cm^{-2}. 0.05wt% Nafion was added to the catalytic layer.

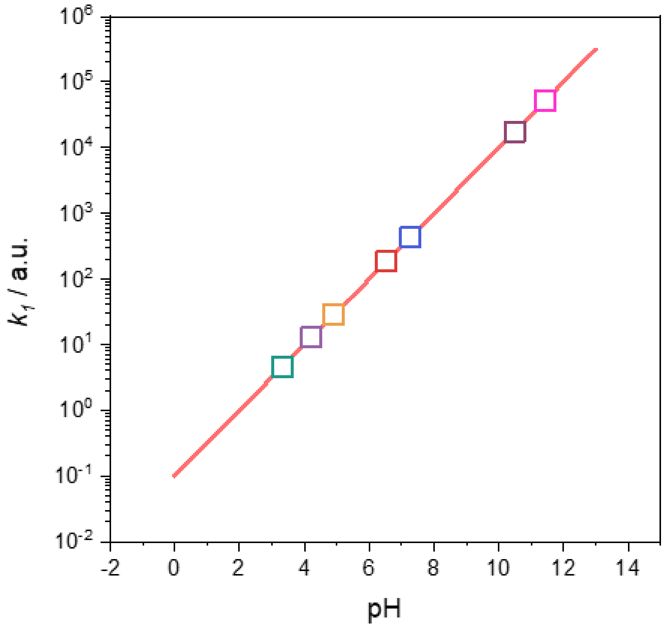

Supplementary Figure 11: The pH effect on the first step of ORR on Au in ionic liquids ($O_2 + e^- + N\text{-}H^+ \Rightarrow OOH + N$) was estimated using Koper's model [15], the detailed method was depicted in Supplementary Methods. The local pH of ionic liquids is calculated from pK_a value of them. As shown in Supplementary Figure 11, the apparent rate constant (k_1) of first ORR step on Au in ionic liquids can increase by two to six orders of magnitude compared to the reaction carried out in acid solution when pH=0. Although, the rate constant of the first step ($O_2 + e^- + H^+ \Rightarrow OOH$) has been suggested to be slightly slower than the second step ($OOH + e^- + H^+ \Rightarrow HOOH$) in acid aqueous solution, the difference is estimated to be less than 2 orders of magnitude [16]. Because the second step is coupled PCET step, which isn't affected by pH [17], k_1 would become much higher than k_2 in ionic liquids, which would make the second step play a more important role in overall kinetics. This suggestion agrees with the previous works in studying oxygen reduction in organic solvent, where the first ET step[18] is about 3 orders of magnitude faster than the second PCET step [19].

Supplementary Table 1: Summary of estimated size and coverage of cations. The predicted and measured enhancement of ORR on Au and Pt were also depicted. The coverage of intermediates (O_{Pt} and OH_{Pt} on Pt) is about 20-30% at ORR relevant potentials[20, 21] and that of cations was estimated to be 17-30% on Pt and 18-32% on Au, we suggested the coverage of cations is comparative with the coverage of ORR intermediates when we consider the ORR intermediates on the surface grabbing proton from ionic liquids. Further, the predict enhancement in intrinsic activity of RDS is higher than measured enhancement in overall reaction rate, indicating the ionic liquids can afford the enhancement observed experimentally, even though the coverage of $[MTBD]^+$ and $[DEMA]^+$ is lower than $[C_4Him]^+$.

Cation	Length / Å	Width / Å	Coverage on Pt	Coverage on Au	Predicted enhancement on Pt (j_0)	Measured enhancement on Pt (j_0)	Predicted enhancement on Au (j_0)	Measured enhancement on Au (j_0)
$[MTBD]^+$	9.1	5.1	17%	18%	5.88	2.33	1.09	1.05
$[DEMA]^+$	8.5	5.1	18%	19%	1.62	1.47	4.07	2.33
$[C_4Him]^+$	6.3	4.1	30%	32%	1	1	1	1

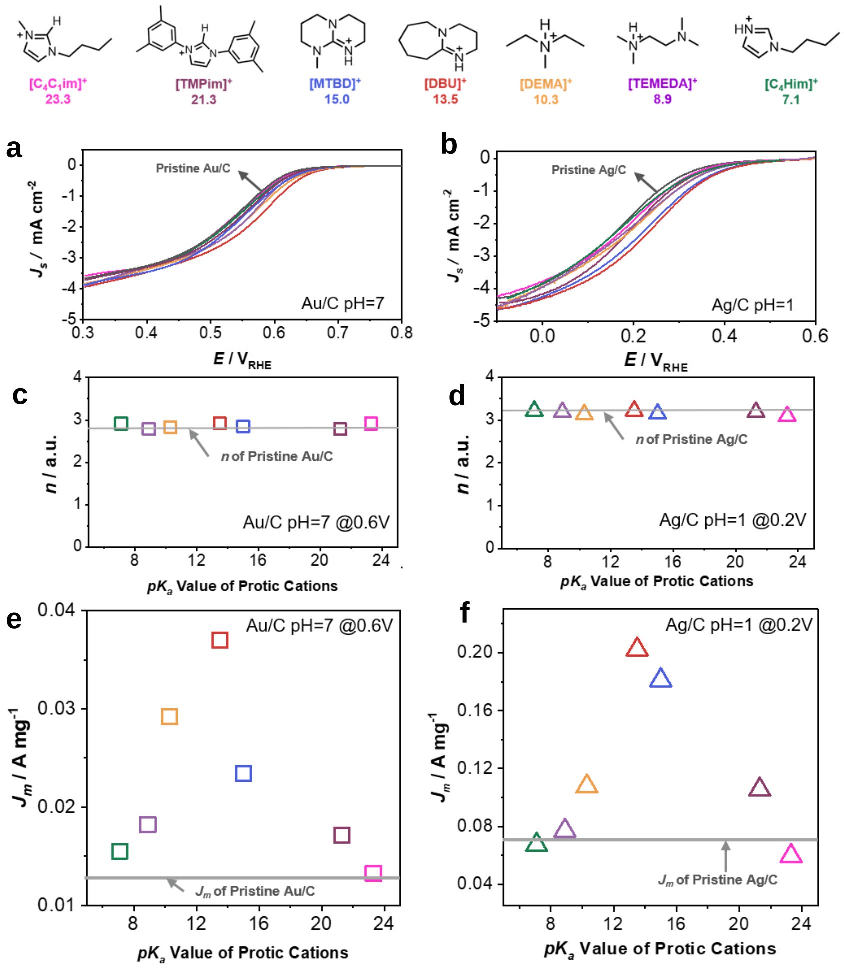

Supplementary Figure 12: pK_a-dependent ORR activity on Au/C measured in O_2-saturated 0.1 M $NaClO_4$ and Ag/C measured in O_2-saturated 0.1 M $HClO_4$, with a scan rate of 10 mV/s and the rotation speed is 1600 rpm. (a and b) Background and *IR* corrected ORR polarization curves of ionic-liquids-modified Au/C (a) and Ag/C (b); (c and d) The number of electrons transferred in ORR process (denoted as *n*) was measured on Au/C (c) and Ag/C (d) by RRDE. *n* was extracted from J_m and J_{H2O2} following the equation that $n = 4 \times \frac{J_m}{J_m + \frac{J_{H_2O_2}}{N_c}}$ (8), N_c is the collection efficiency of RRDE, which is 0.37 in these measurements; (e and f) The relationship between the enhancement in ORR mass specific kinetic currents on ionic-liquids-modified Au/C (e), Ag/C (f) as a function of the pK_a value of protic cations in ionic liquids. The loading of Au and Ag was controlled at 40 μg·cm^{-2}. 0.05wt% Nafion was added to the catalytic layer.

Supplementary Note 1: The ORR polarization curves of ionic-liquid-modified Au/C in 0.1M $NaClO_4$ are depicted in Supplementary Figure 12 (a). ORR activity was found depend on pK_a value of cations. The number of electrons transferred in ORR (*n*) is depicted in Supplementary Figure 12 (c), showing that *n* of Au/C and ionic-liquid-modified Au/C is within 2.7-2.9, which reveals that Au/C in the natural electrolyte catalyse ORR via both two-electron and four-electron pathway. The relationship between pK_a value of cations and ORR enhancement of Au/C is depicted in Supplementary Figure 12 (e). The maximum ORR activity enhancement for Au/C at pH=7 was found for [DBU][NTf_2] with pK_a of 13.5, of which the pK_a is higher than [DEMA][NTf_2] (pK_a=10.3) for two-electron pathway and lower than [MTBD][NTf_2] (pK_a=15.0) for four-electron pathway. Besides, the max enhancement for ionic liquid modified Au/C (Supplementary Figure 12 (e)) was found around 2.6 time, which is slightly lower than the max enhancement of Au/C measured at pH=1 depicted in Fig. 1 (about 5 times). The reason for the decrease in maximum enhancement might be originated from the compromising enhancement of [DBU][NTf_2] for both two-electron and four-electron pathway.

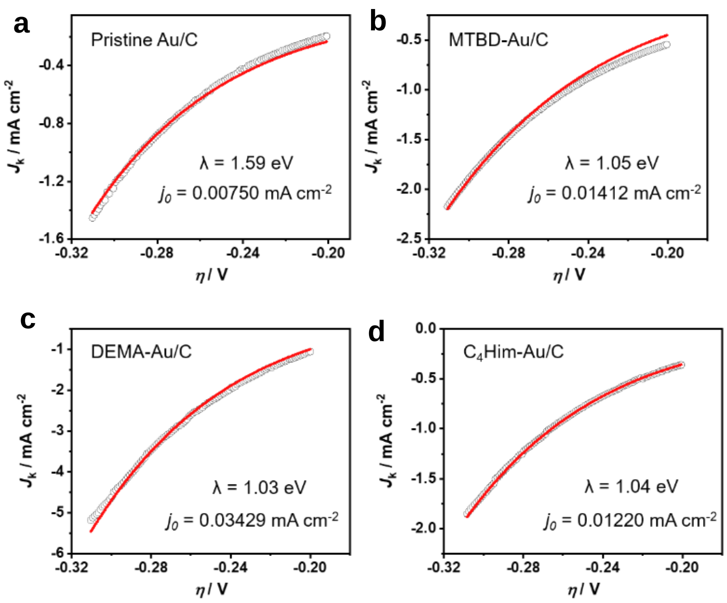

Supplementary Figure 13: ORR kinetic current density of pristine Au/C (a) and Au/C modified with [MTBD][NTf_2] (b), [DEMA][NTf_2] (c) and [C_4Him][NTf_2] (d) measured in oxygen saturated 0.1M $HClO_4$ (Supplementary Figure 3b) is plotted against overpotential (η) and fitted to the MHC equation. The reorganization energy extracted from MHC equation is depicted in figures. The details of analysis were depicted in Supplementary Methods. The equilibrium potential of ORR on Au was defined as the equilibrium potential of oxygen reducing to H_2O_2 ($O_2 + 2H^+ + 2e^- \rightarrow H_2O_2$, 0.68 V_{RHE}). The results show that the reorganization energy in aqueous solution is 1.59 eV and in ionic liquids are around 1 eV. Therefore, the hydrophobic environment created by ionic liquids (static dielectric constant is around 12-15 in bulk[12, 22]) actually reduce the dielectric constant of catalysts' surface compared with aqueous environment (static dielectric constant is 78.5 in bulk[23]) and, consequently, reduce the reorganization energy for ORR and increase ORR activity. Moreover, the reorganization energy for different ionic liquids is similar, since the dielectric constant is similar for the ionic liquids we studied, of which the anion is TFSI [12, 22]. Therefore, our discussion in manuscript focused on the effect of hydrogen bonding structure on the pre-exponential factor and exchange current density of ORR by comparing PCET kinetics of different ionic liquids.

Supplementary Note 2: Besides, we could extract the dielectric constant in local reaction environment by Born model from reorganization energy as following equation,

$$\lambda_o = \frac{e^2}{8\pi\varepsilon_0 k_B T}\left(\frac{1}{a_0} - \frac{1}{2d}\right)\left(\frac{1}{\varepsilon_{op}} - \frac{1}{\varepsilon_s}\right) \qquad (9)$$

where ε_0 is the permittivity of free space, a_0 as the effective radius of the reactant, d as the distance from the redox center to the surface of the electrode, ε_{op} the optical dielectric constant and ε_s as the static dielectric constant of the electrolyte near the electrified interface. The radius of H_2O_2 molecule (1.3 Å) was adopted as the radius of redox species for a_0, the distance d between redox and the Au electrode was found to be 3.0 Å in previous work[24], the optical dielectric constant is 1.8 for water and around 2.0 for ionic liquids. It is also need to mention that the reorganization energy we extracted from MHC theory (λ) is compose of inner and outer components, $\lambda = \lambda_i + \lambda_o$ (10), and we need to obtain λ_o for fitting Born Model by subtracting λ_i from λ. The inner component of reorganization energy for ORR on Au can be estimated by the George-Griffith model[25, 26] as following equation,

$$\lambda_i = 2n\left[\frac{f_z f_{z+1}}{f_z + f_{z+1}}(\Delta r)^2\right] \qquad (11)$$

where having f_i as force constant described by $4\pi^2 m_L C^2 \omega_i^2 / \mathcal{N}_A$, Δr is the change in bond length between oxidized and reduced forms, n is the number of ligands, m_L is the molar mass of the ligand, C is the speed of light in vacuum and $\mathcal{N}_A$ is the Avogadro constant. The change in O-H bond length (Δr) could be measured in DFT models of oxidized species (HO**O···H**-N, ~2 Å) and reduced species (HO**O-H**···N, ~1 Å), the inner reorganization energy was calculated to be 0.38 - 0.43 eV for the ion liquids of three different cations and 0.26 eV for water. Consequently, we can estimate that the dielectric constants of ionic liquid on Au surface is around 2.5 - 2.6, which is evident lower than that of water on Au (~3.8) under ORR condition. Therefore, we confirm that the increasing hydrophobicity of ionic liquids can reduce the dielectric constant in local reaction environment and consequently reduce the reorganization energy of ORR from those in acid.

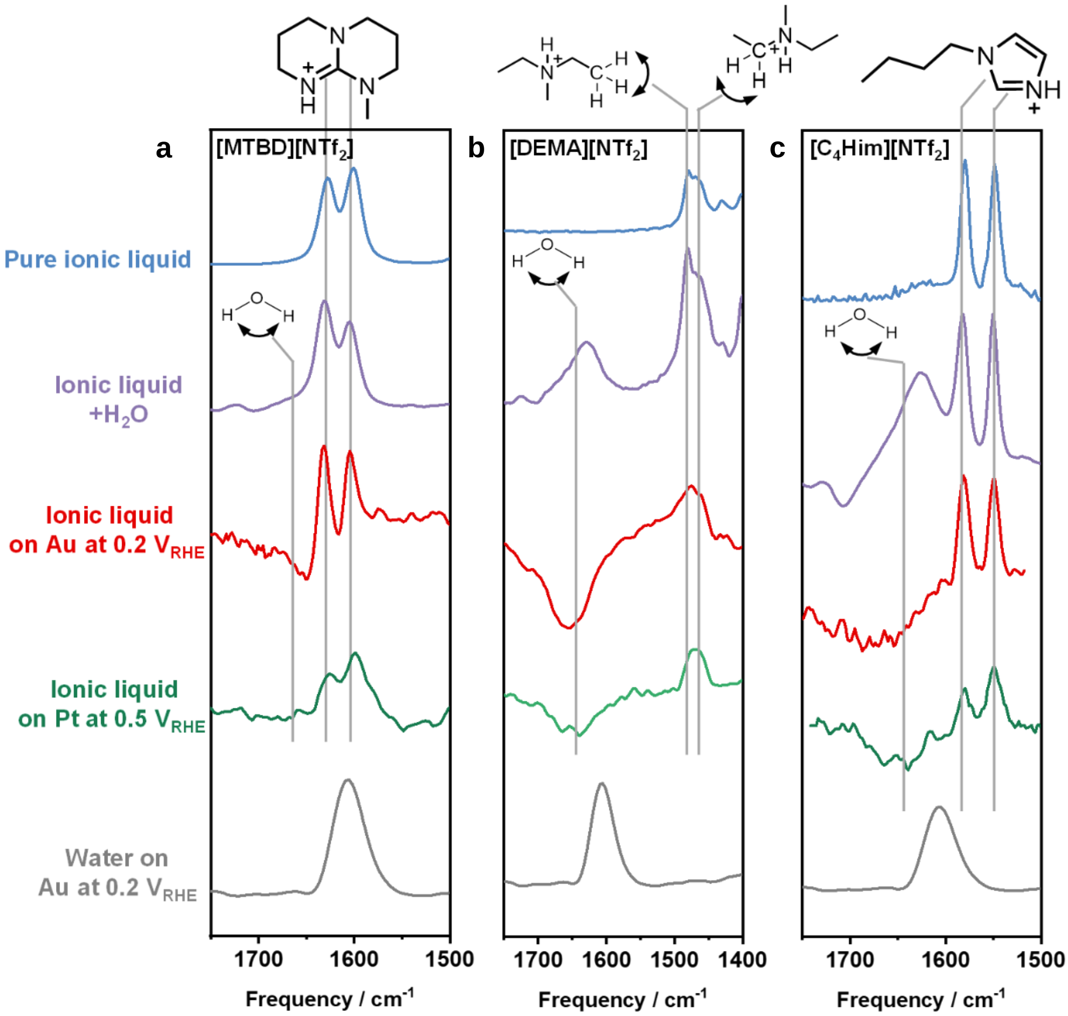

Supplementary Figure 14: The IR spectra of cations (blue) for pristine ionic liquids ([MTBD][NTf$_2$] (a), [DEMA][NTf$_2$] (b) and [C$_4$Him][NTf$_2$] (c)), ionic liquids with 0.5 M water (purple), ORR on ionic-liquid-modified Au at 0.2 V$_{RHE}$ (red), ORR on ionic liquid modified Pt at 0.5 V$_{RHE}$ (green) and the HOH bending signal of water on bare Au surface at 0.2 V$_{RHE}$ (gray). The cumulative number of 256 was used at a 4 cm^{-1} resolution. Spectra were subtracted with respect to a reference spectrum obtained at OCV in 0.1 M $HClO_4$.

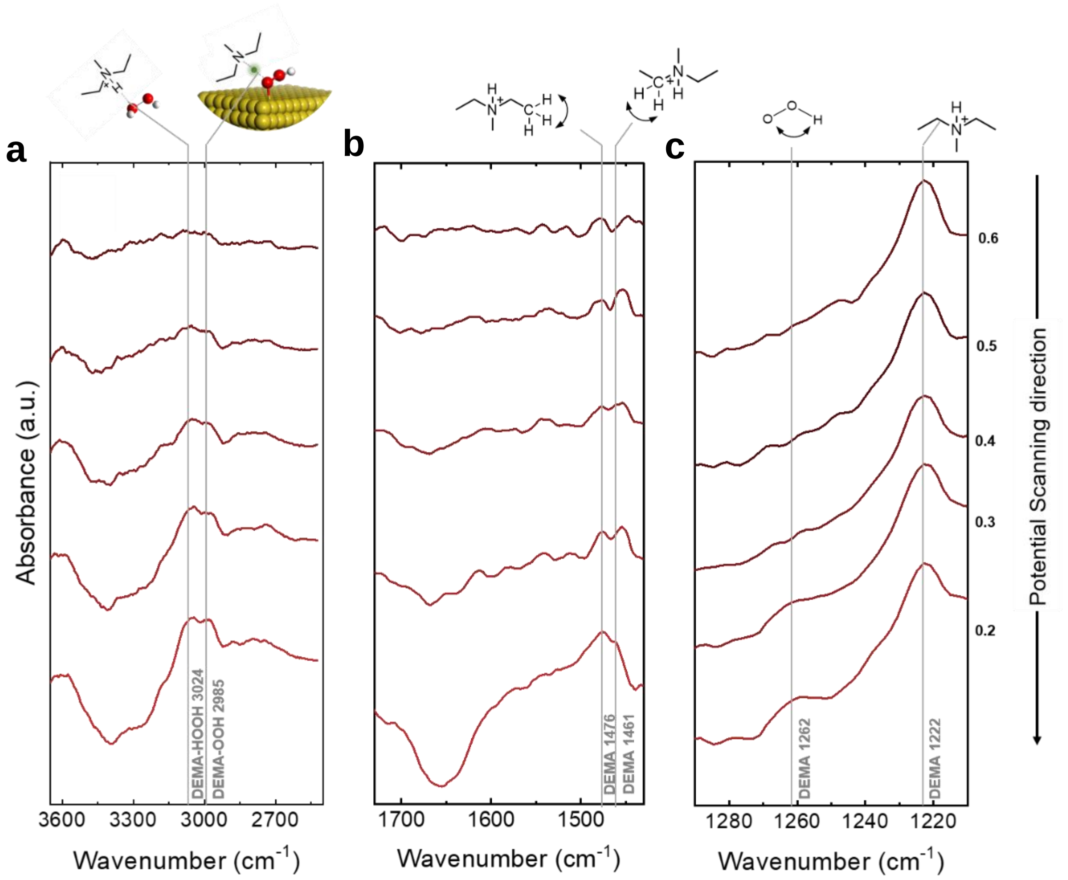

Supplementary Figure 15: *In-situ* ATR-SEIRAS measurement on a [DEMA][NTf_2]-modified Au electrode in oxygen-saturated 0.1 M $HClO_4$. (a) X-H (X=N, O) stretching region, the molecular schematic represents the H-bond specie formed between [DEMA]$^+$ and OOH; (b) H-C-H bending region and (c) O-O-H bending region were obtained during potential steps swept from 0.2 V_{RHE} to 0.6 V_{RHE} in 0.1 M $HClO_4$. The cumulative number of 256 was used at a 4 cm^{-1} resolution. Spectra were subtracted with respect to a reference spectrum obtained at OCV in 0.1 M $HClO_4$.

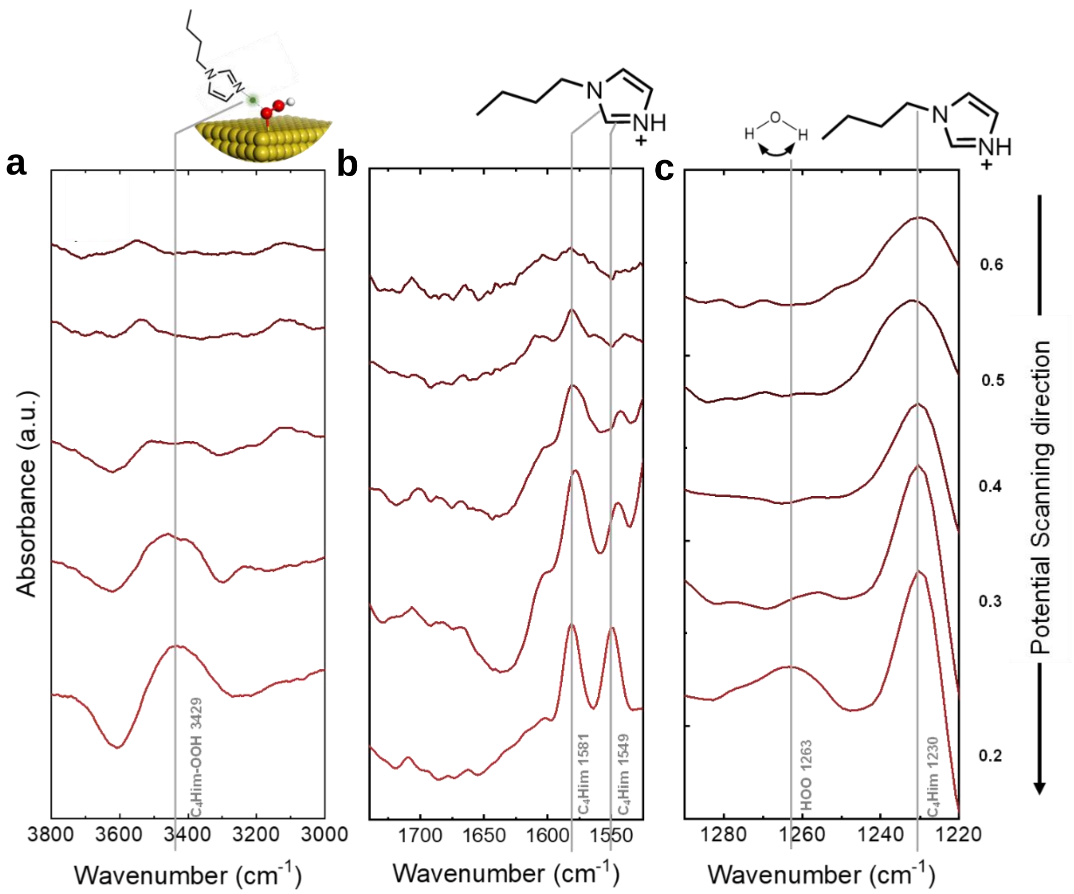

Supplementary Figure 16: *In-situ* ATR-SEIRAS measurement on a [C_4Him][NTf_2]-modified Au electrode in oxygen-saturated 0.1 M $HClO_4$. (a) X-H (X=N, O) stretching region, the molecular schematic represents the H-bond specie formed between $[C_4Him]^+$ and OOH; (b) C=N stretching region and (c) O-O-H bending region were obtained during potential steps swept from 0.2 V_{RHE} to 0.6 V_{RHE} in 0.1 M $HClO_4$. The cumulative number of 256 was used at a 4 cm^{-1} resolution. Spectra were subtracted with respect to a reference spectrum obtained at OCV in 0.1 M $HClO_4$.

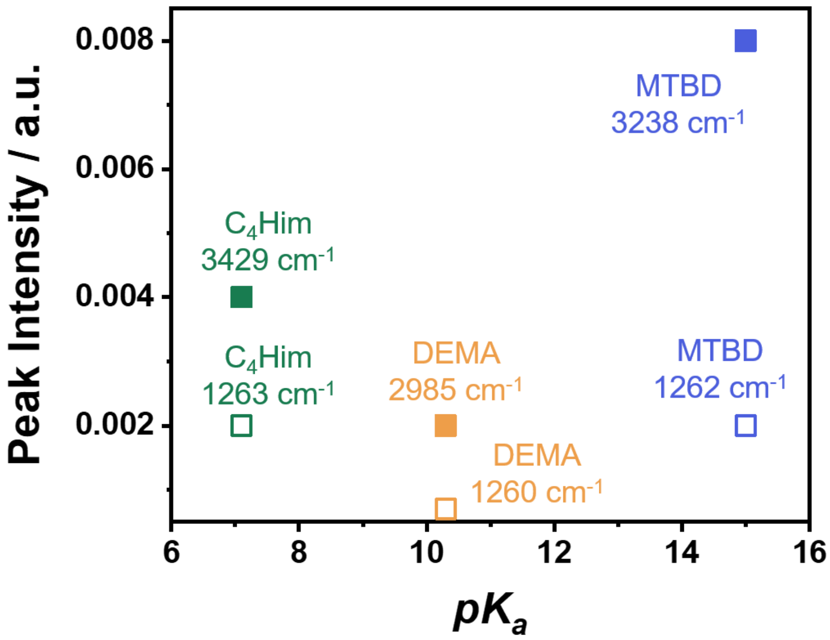

Supplementary Figure 17: The peak intensity of N-H stretching (solid square) and O-O-H bending (open square) of [MTBD][NTf_2]-modified (blue, Fig. 2b, c), [DEMA][NTf_2]-modified (yellow, Supplementary Figure 15) and [C_4Him][NTf_2]-modified (green, Supplementary Figure 16) Au electrode at 0.2V_{RHE} in 0.1M $HClO_4$. The cumulative number of 256 was used at a 4 cm^{-1} resolution.

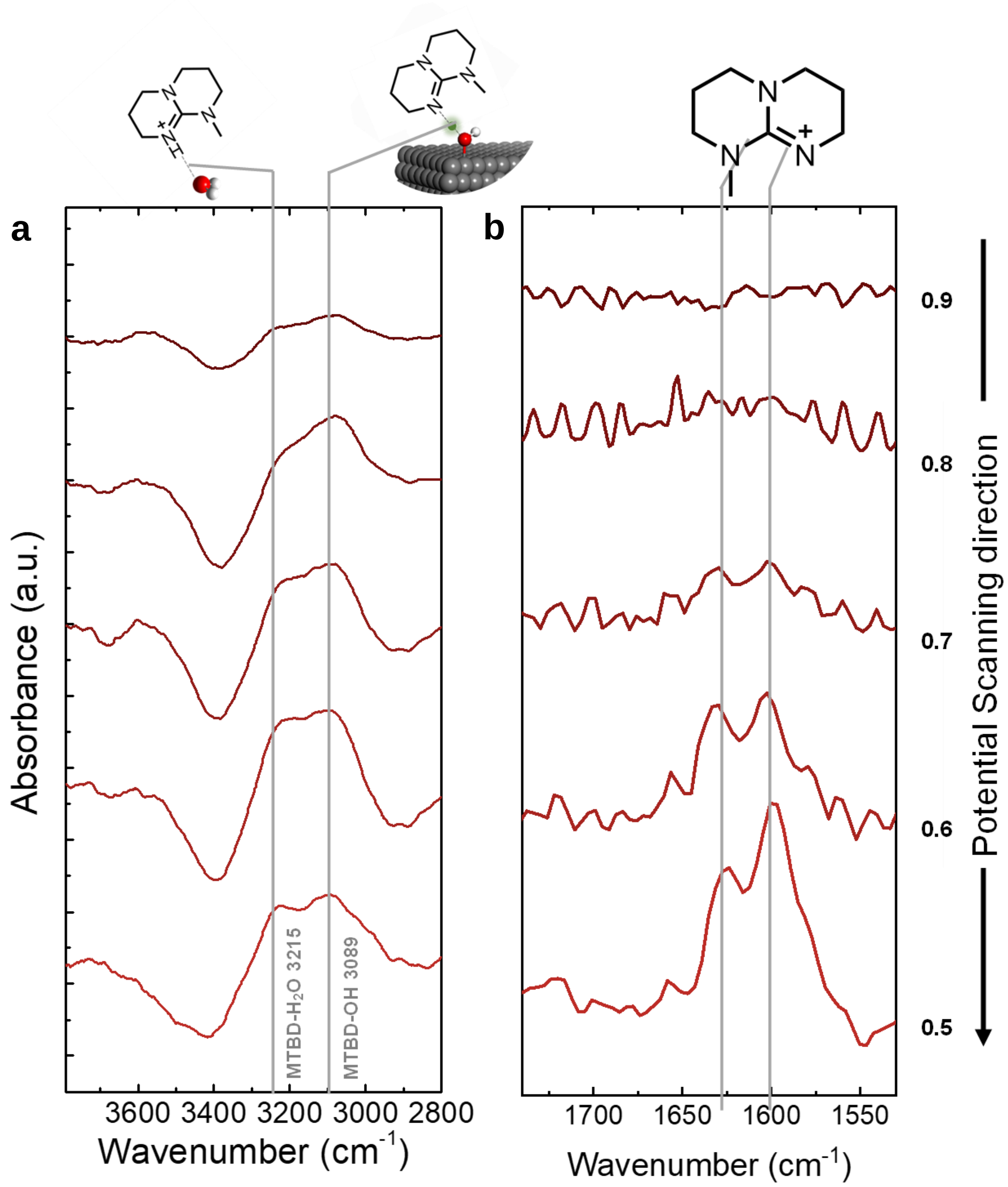

Supplementary Figure 18: *In-situ* ATR-SEIRAS measurement on a [MTBD][NTf_2]-modified Pt electrode modified by [MTBD][NTf_2] in oxygen-saturated 0.1 M $HClO_4$. (a) X-H (X=N, O) stretching region, the molecular schematic represents the H-bond specie formed between $[MTBD]^+$ and OH; (b) C=N stretching region were obtained during potential steps swept from 0.5 V_{RHE} to 0.9 V_{RHE} in 0.1 M $HClO_4$. The cumulative number of 256 was used at a 4 cm^{-1} resolution. Spectra were subtracted with respect to a reference spectrum obtained at OCV in 0.1 M $HClO_4$.

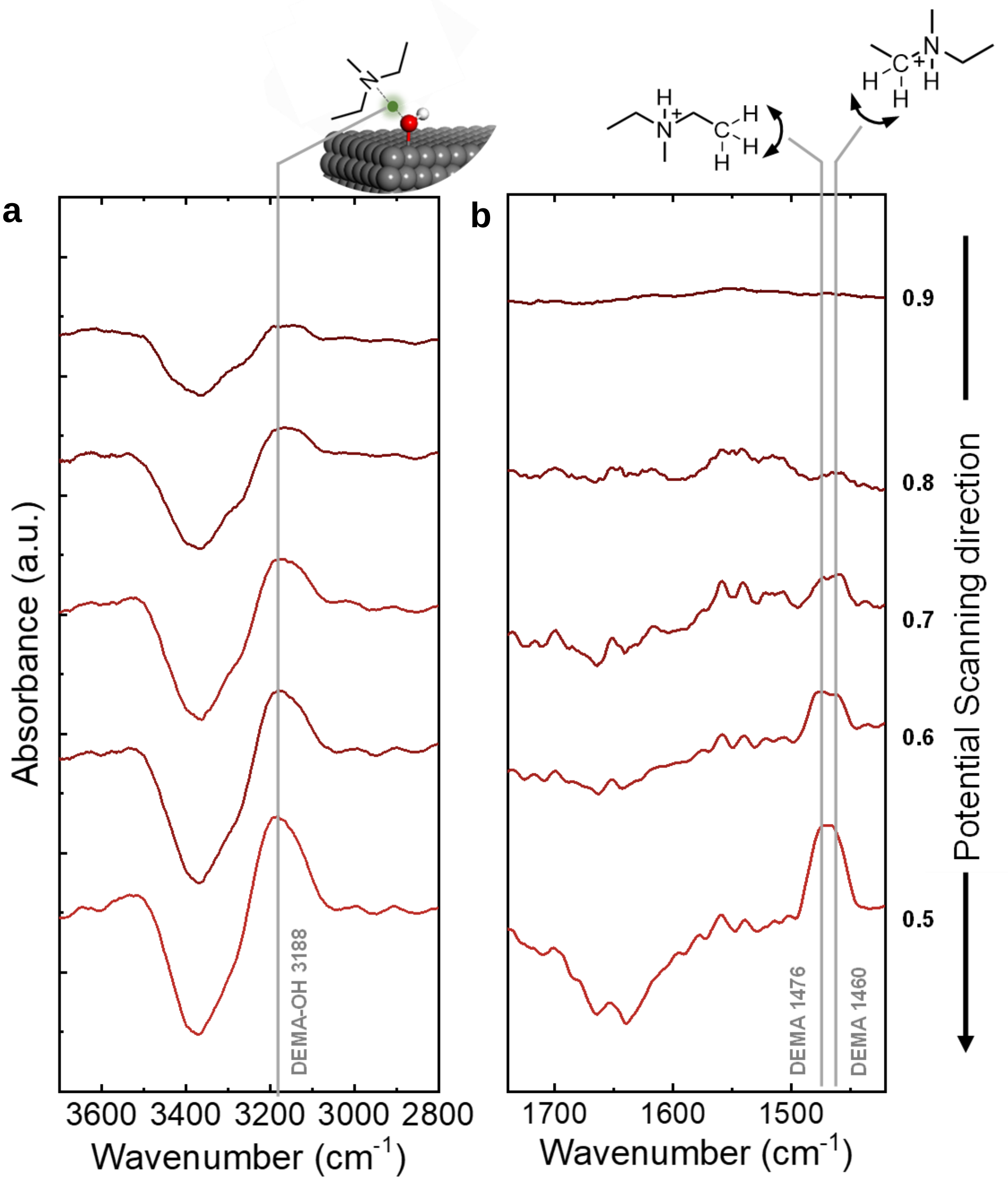

Supplementary Figure 19: *In-situ* ATR-SEIRAS measurement on a [DEMA][NTf$_2$]-modified Pt electrode in oxygen-saturated 0.1 M $HClO_4$. (a) X-H (X=N, O) stretching region, the molecular schematic represents the H-bond specie formed between [DEMA]$^+$ and OH (b) H-C-H bending region were obtained during potential steps swept from 0.5 V_{RHE} to 0.9 V_{RHE} in 0.1 M $HClO_4$. The cumulative number of 256 was used at a 4 cm^{-1} resolution. Spectra were subtracted with respect to a reference spectrum obtained at OCV in 0.1 M $HClO_4$.

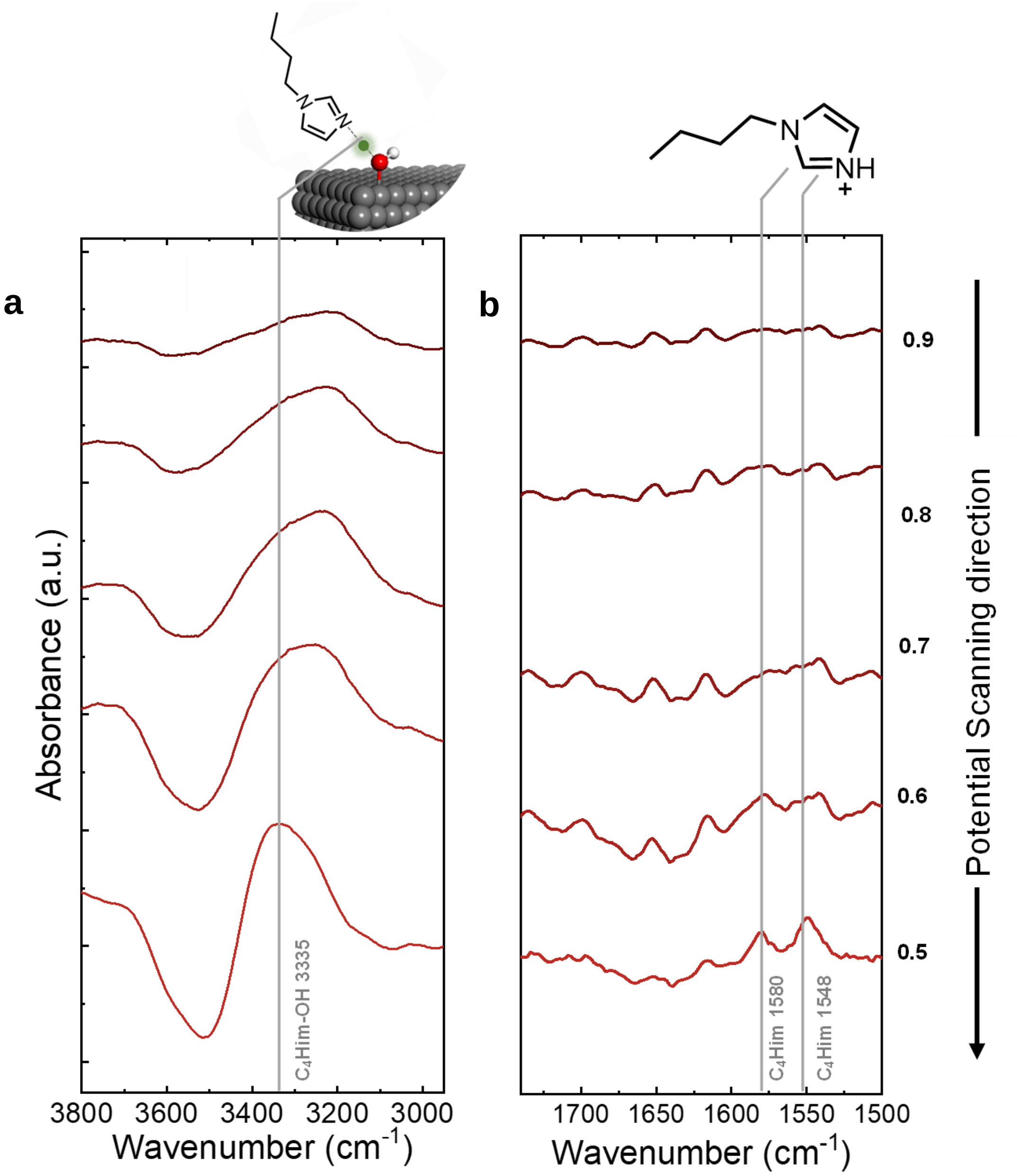

Supplementary Figure 20: *In-situ* ATR-SEIRAS measurement on a [C_4Him][NTf_2]-modified Pt electrode in oxygen-saturated 0.1 M $HClO_4$. (a) X-H (X=N, O) stretching region, the molecular schematic represents the H-bond specie formed between [C_4Him]$^+$ and OH; (b) C=N stretching region were obtained during potential steps swept from 0.5 V_{RHE} to 0.9 V_{RHE} in 0.1 M $HClO_4$. The cumulative number of 256 was used at a 4 cm^{-1} resolution. Spectra were subtracted with respect to a reference spectrum obtained at OCV in 0.1 M $HClO_4$.

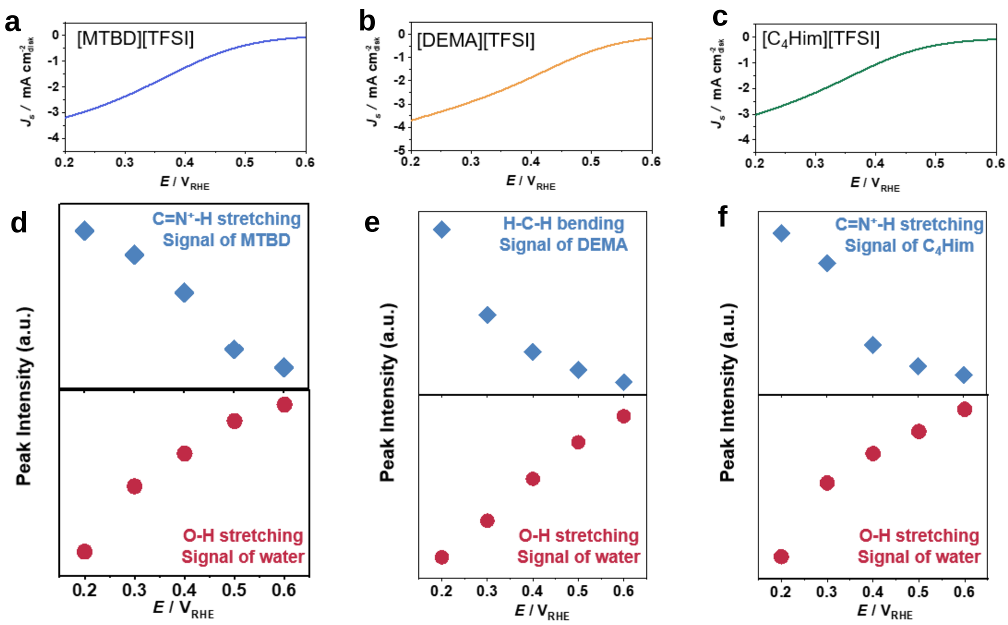

Supplementary Figure 21: (a, b, c) ORR polarization curves of [MTBD][TFSI], [DEMA][TFSI] and [C_4Him][TFSI] measured in O_2-saturated 0.1 M $HClO_4$, with a scan rate of 10 mV/s and the rotation speed is 1600 rpm; (d, e, f) the IR peak intensity of cations (blue) and water (red) at ORR relevant potentials. The cumulative number of 256 was used at a 4 cm^{-1} resolution. Spectra were subtracted with respect to a reference spectrum obtained at OCV in 0.1 M $HClO_4$.

Supplementary Table 2: The simulated and experimental stretching frequency for H-bonded species formed between protic cations ($[MTBD]^+$, $[DEMA]^+$ and $[C_4Him]^+$) and ORR intermediates/products. The spectra of X-H (X=N, O) stretching region of $[MTBD][NTf_2]$-modified Au, $[DEMA][NTf_2]$-modified Au, $[C_4Him][NTf_2]$-modified Au, $[MTBD][NTf_2]$-modified Pt, $[DEMA][NTf_2]$-modified Pt and $[C_4Him][NTf_2]$-modified Pt were depicted in Fig. 3. *In situ* ATR-SEIRA measurement on an ionic-liquid-modified Au and a Pt electrode in 0.1 M $HClO_4$. The spectra were acquired at 0.2 V_{RHE} for Au and 0.5V_{RHE} for Pt. The cumulative number of 256 was used at a 4 cm^{-1} resolution.

Au-IL	Frequency/cm^{-1} (Simulated)	Frequency/cm^{-1} (Experimental)
$[MTBD]^+$-OOH	3267	3240
$[DEMA]^+$-OOH	3110	2985
$[DEMA]^+$-HOOH	3204	3024
$[C_4Him]^+$-OOH	3371	3429

Pt-IL	Frequency/cm^{-1} (Simulated)	Frequency/cm^{-1} (Experimental)
$[MTBD]^+$-OH	3198	3089
$[MTBD]^+$-H_2O	3277	3215
$[DEMA]^+$-OH	3253	3188
$[C_4Him]^+$-OH	3332	3335

Supplementary Table 3. Summary of water solubility of different ionic liquids and corresponding ORR activity on Au/C and Pt/C. The water solubility was measured by Karl Fischer titration. Error bars represent standard deviations (SDs) of at least three independent measurements.

Cations	C_4C_1im	TMPim	MTBD	DBU	DEMA	TEMEDA	C_4Him
Water solubility (M)	0.49±0.02	0.45±0.03	1.29±0.03	1.25±0.02	1.19±0.02	0.78±0.03	0.59±0.02
ORR Activity on Au (mA cm^{-2})	0.074±0.005	0.078±0.002	0.113±0.013	0.200±0.019	0.237±0.033	0.150±0.015	0.089±0.012
ORR Activity on Pt (mA cm^{-2})	0.426±0.036	0.554±0.045	0.649±0.052	0.508±0.038	0.362±0.033	0.270±0.028	0.177±0.013

Supplementary Table 4. Summary of exchange current density, preexponential factor and reorganization energy of ORR on Au/C, which extracted from MHC equation.

	j_0 / mA cm^{-2}	A	λ / eV
[MTBD][NTf_2]	0.01412	118.77	1.05
[DEMA][NTf_2]	0.03429	250.25	1.03
[C_4Him][NTf_2]	0.01220	90.61	1.04
0.1M $HClO_4$	0.00750	11669.70	1.59

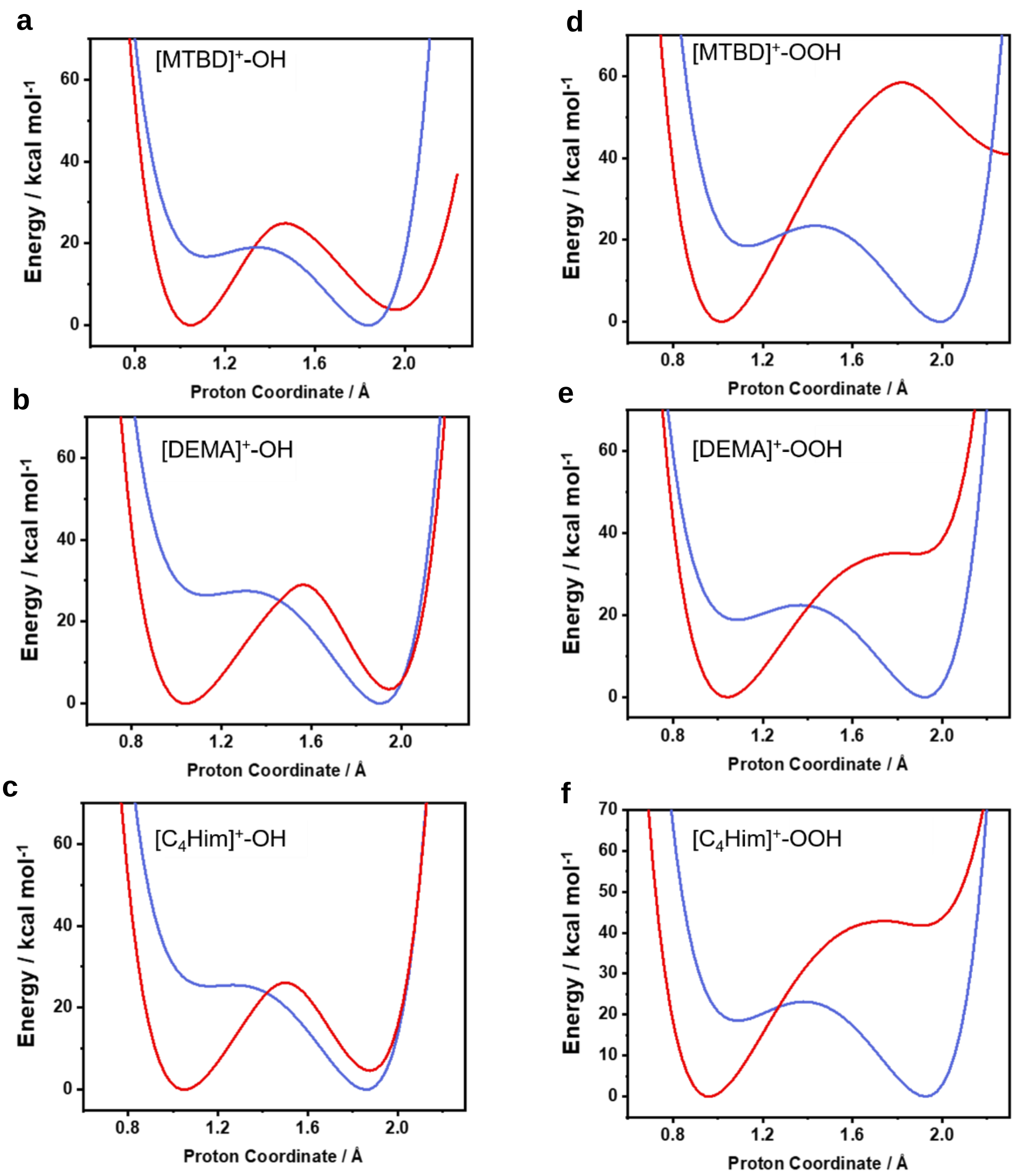

Supplementary Figure 22: Proton potential scanned along the proton axis in the H-bonded interface of different H-bond species in reactant (red) and product (blue) states, which are composed of ionic liquid cations and ORR intermediates, $[MTBD]^+$-OH (a), $[DEMA]^+$-OH (b), $[C_4Him]^+$-OH (c), $[MTBD]^+$-OOH (d), $[DEMA]^+$-OOH (e) and $[C_4Him]^+$-OOH (f). The 1D proton potentials were scanned using a reported method [5] and the details were depicted in Supplementary Methods.

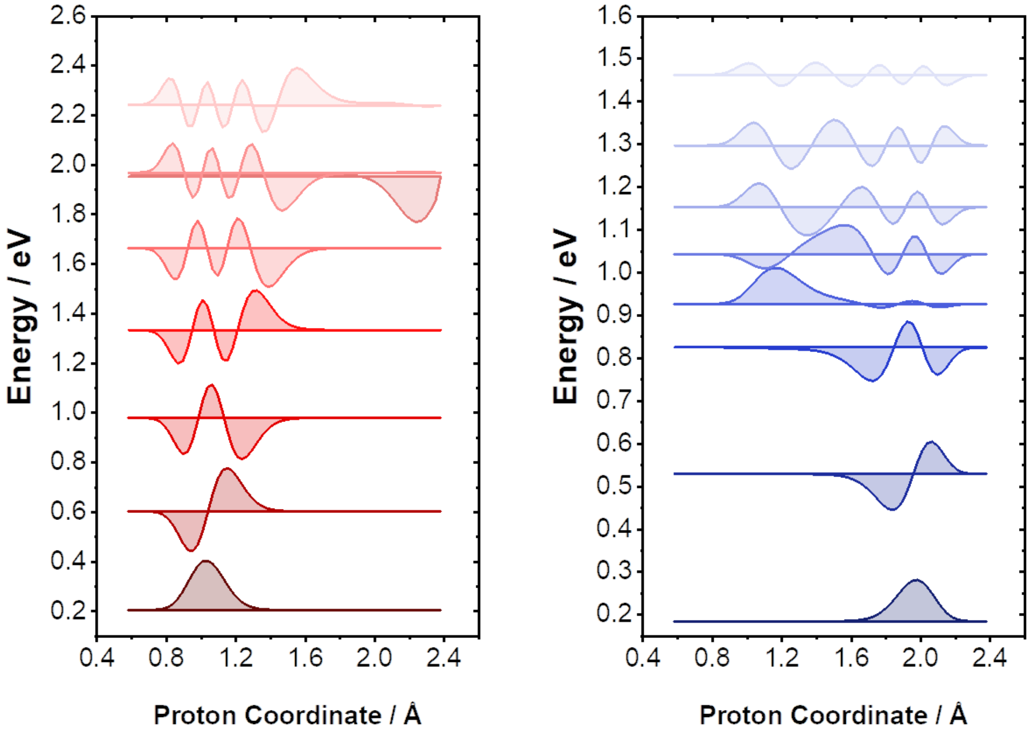

Supplementary Figure 23: Proton vibronic wavefunction and energy levels of $[MTBD]^+$-OOH in different vibronic states of reactant (red) and product (blue), which were calculated for different H-bonded species by solving 1D the one-dimensional Schrödinger equation numerically based on the proton potential obtained in the former part, using the Fourier Grid Hamiltonian Multiconfigurational Self-Consistent-Field (FGH-MCSCF) method developed by Hammes-Schiffer group [8, 9]. The details were depicted in Supplementary Methods.

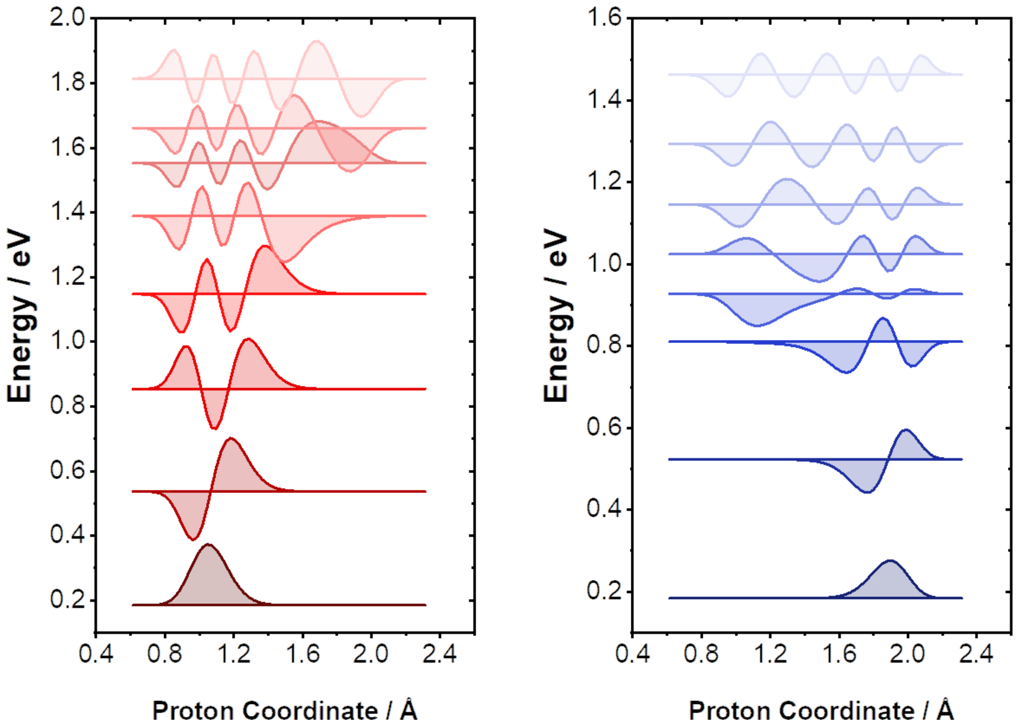

Supplementary Figure 24: Proton vibronic wavefunction and energy levels of $[DEMA]^+$-OOH in different vibronic states of reactant (red) and product (blue), which were calculated for different H-bonded species by solving 1D the one-dimensional Schrödinger equation numerically based on the proton potential obtained in the former part, using the Fourier Grid Hamiltonian Multiconfigurational Self-Consistent-Field (FGH-MCSCF) method developed by Hammes-Schiffer group [8, 9]. The details were depicted in Supplementary Methods.

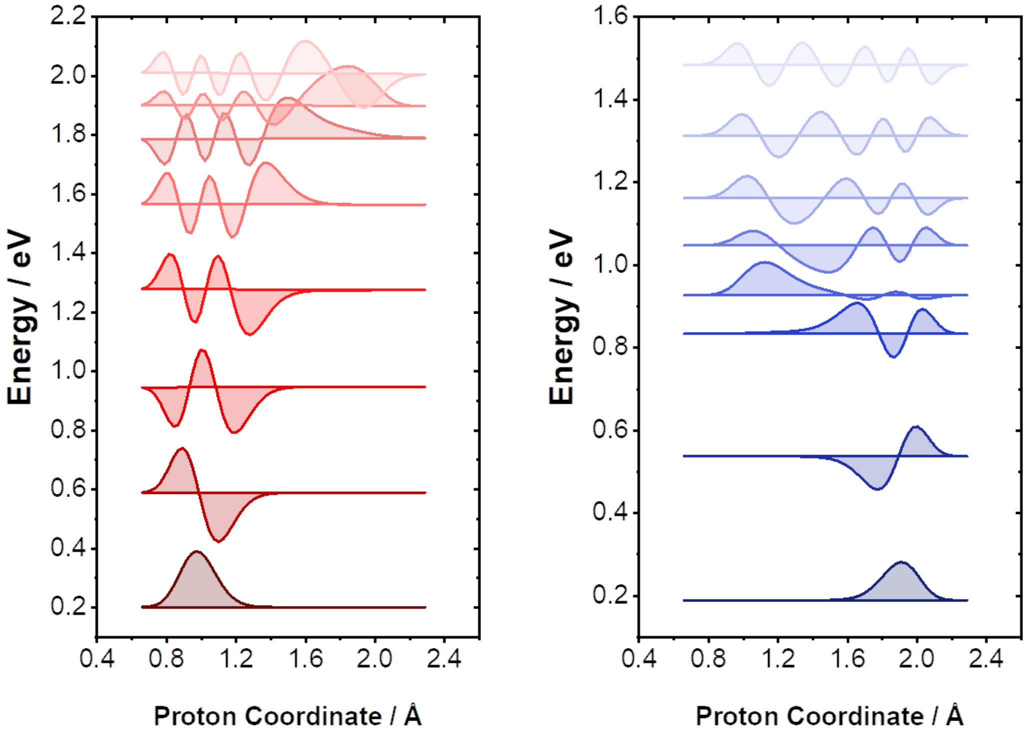

Supplementary Figure 25: Proton vibronic wavefunction and energy levels of $[C_4Him]^+$-OOH in different vibronic states of reactant (red) and product (blue), which were calculated for different H-bonded species by solving 1D the one-dimensional Schrödinger equation numerically based on the proton potential obtained in the former part, using the Fourier Grid Hamiltonian Multiconfigurational Self-Consistent-Field (FGH-MCSCF) method developed by Hammes-Schiffer group [8, 9]. The details were depicted in Supplementary Methods.

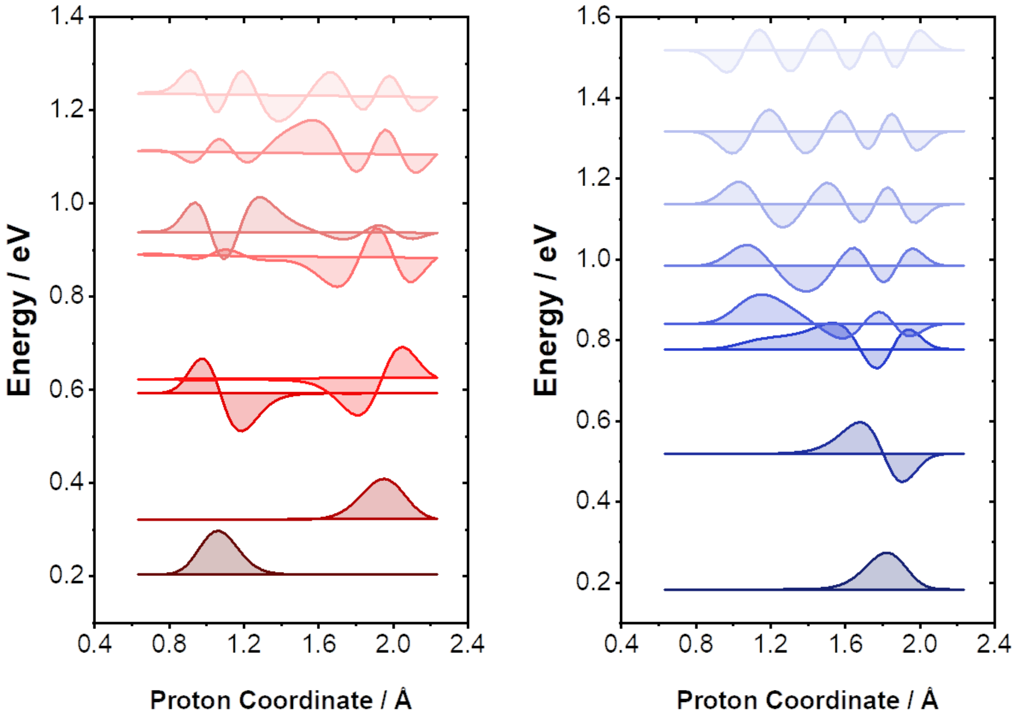

Supplementary Figure 26: Proton vibronic wavefunction and energy levels of $[MTBD]^{+}$-OH in different vibronic states of reactant (red) and product (blue), which were calculated for different H-bonded species by solving 1D the one-dimensional Schrödinger equation numerically based on the proton potential obtained in the former part, using the Fourier Grid Hamiltonian Multiconfigurational Self-Consistent-Field (FGH-MCSCF) method developed by Hammes-Schiffer group [8, 9]. The details were depicted in Supplementary Methods.

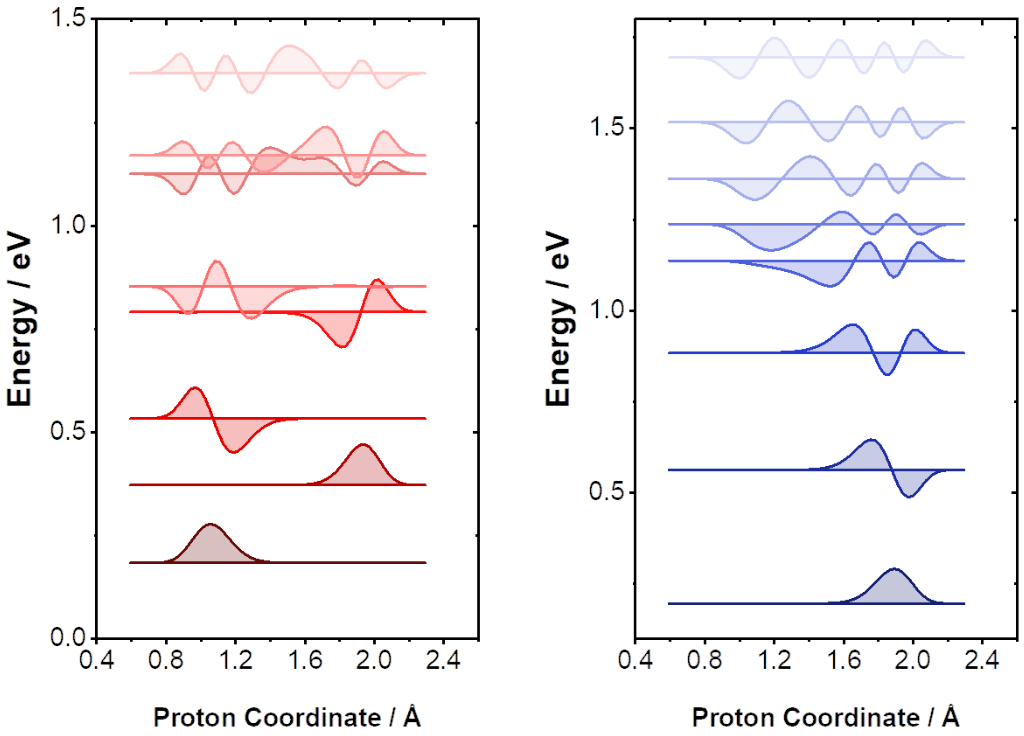

Supplementary Figure 27: Proton vibronic wavefunction and energy levels of $[DEMA]^{+}$-OH in different vibronic states of reactant (red) and product (blue), which were calculated for different H-bonded species by solving 1D the one-dimensional Schrödinger equation numerically based on the proton potential obtained in the former part, using the Fourier Grid Hamiltonian Multiconfigurational Self-Consistent-Field (FGH-MCSCF) method developed by Hammes-Schiffer group [8, 9]. The details were depicted in Supplementary Methods.

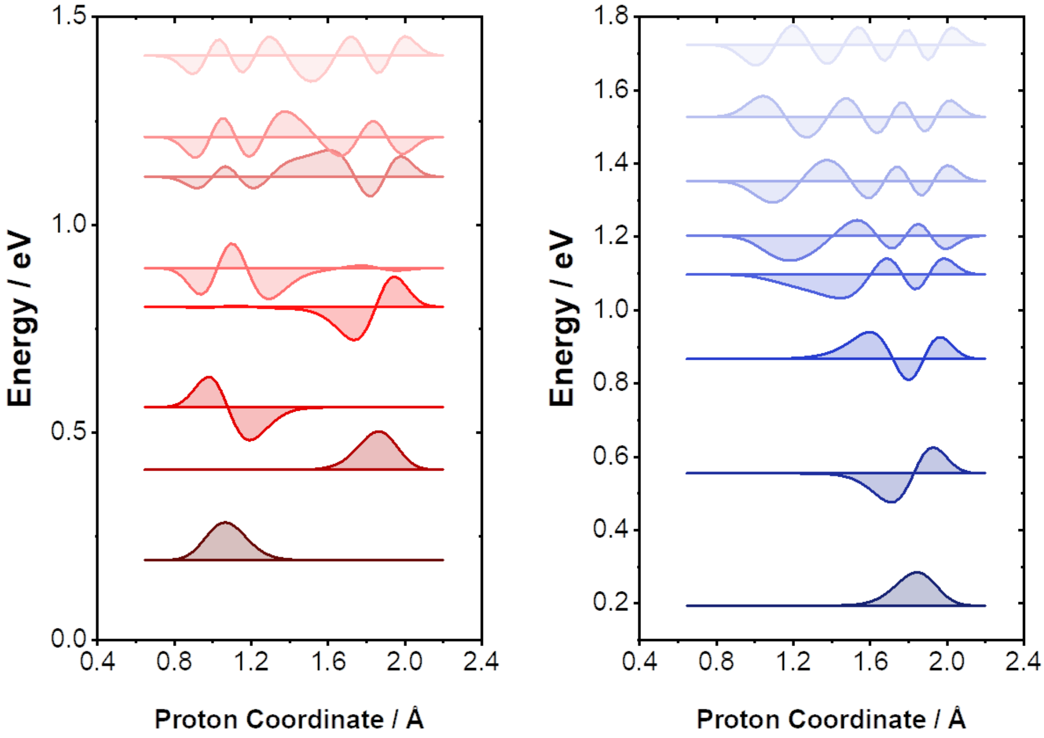

Supplementary Figure 28: Proton vibronic wavefunction and energy levels of $[C_4Him]^+$-OH in different states vibronic states of reactant (red) and product (blue), which were calculated for different H-bonded species by solving 1D the one-dimensional Schrödinger equation numerically based on the proton potential obtained in the former part, using the Fourier Grid Hamiltonian Multiconfigurational Self-Consistent-Field (FGH-MCSCF) method developed by Hammes-Schiffer group [8, 9]. The details were depicted in Supplementary Methods.

Supplementary Table 5: The contribution to the overall rate constant of PCET between cations and OOH. The different quantum states of reactant (μ = 0-7) present in different columns and the different quantum states of product (ν = 0-7) present in different rows. We found (0, 3) showed the highest rate constant for three different cations, where (0, 3) of [C_4Him]-OOH and [MTBD]-OOH account for more than 90% in overall rate constant and (0, 3) of [DEMA]-OOH account for 53% in overall rate constant. About 35% of the overall rate constant of [DEMA]-OOH is contributed from (0, 0) state.

$[MTBD]^+$-OOH

Contribution%	0	1	2	3	4	5	6	7
0	1.0	0.0	0.0	0.0	0.0	0.0	0.0	0.0
1	1.0	0.0	0.0	0.0	0.0	0.0	0.0	0.0
2	1.6	0.0	0.0	0.0	0.0	0.0	0.0	0.0
3	94.0	2.0	0.0	0.0	0.0	0.0	0.0	0.0
4	0.3	0.0	0.0	0.0	0.0	0.0	0.0	0.0
5	0.0	0.0	0.0	0.0	0.0	0.0	0.0	0.0
6	0.0	0.0	0.0	0.0	0.0	0.0	0.0	0.0
7	0.0	0.0	0.0	0.0	0.0	0.0	0.0	0.0

$[DEMA]^+$-OH

Contribution%	0	1	2	3	4	5	6	7
0	35.2	0.7	0.0	0.0	0.0	0.0	0.0	0.0
1	7.8	0.4	0.0	0.0	0.0	0.0	0.0	0.0
2	2.5	0.1	0.0	0.0	0.0	0.0	0.0	0.0
3	52.6	0.5	0.0	0.0	0.0	0.0	0.0	0.0
4	0.2	0.0	0.0	0.0	0.0	0.0	0.0	0.0
5	0.0	0.0	0.0	0.0	0.0	0.0	0.0	0.0
6	0.0	0.0	0.0	0.0	0.0	0.0	0.0	0.0
7	0.0	0.0	0.0	0.0	0.0	0.0	0.0	0.0

$[C_4Him]^+$-OH

Contribution%	0	1	2	3	4	5	6	7
0	2.5	0.0	0.0	0.0	0.0	0.0	0.0	0.0
1	1.7	0.0	0.0	0.0	0.0	0.0	0.0	0.0
2	2.7	0.1	0.0	0.0	0.0	0.0	0.0	0.0
3	90.0	2.7	0.0	0.0	0.0	0.0	0.0	0.0
4	0.3	0.0	0.0	0.0	0.0	0.0	0.0	0.0
5	0.0	0.0	0.0	0.0	0.0	0.0	0.0	0.0
6	0.0	0.0	0.0	0.0	0.0	0.0	0.0	0.0
7	0.0	0.0	0.0	0.0	0.0	0.0	0.0	0.0

Supplementary Table 6. The contribution to the overall rate constant of PCET between cations and OH. The different quantum states of reactant (μ = 0-7) present in different columns and the different quantum states of product (ν = 0-7) present in different rows. For PCET between ionic liquid and OH (ORR process on Pt), (1, 0) is the contributing state, which account for more than 99% in overall rate constant.

$[MTBD]^+$-OH

Contribution%	0	1	2	3	4	5	6	7
0	0.0	99.9	0.0	0.1	0.0	0.0	0.0	0.0
1	0.0	0.0	0.0	0.0	0.0	0.0	0.0	0.0
2	0.0	0.0	0.0	0.0	0.0	0.0	0.0	0.0
3	0.0	0.0	0.0	0.0	0.0	0.0	0.0	0.0
4	0.0	0.0	0.0	0.0	0.0	0.0	0.0	0.0
5	0.0	0.0	0.0	0.0	0.0	0.0	0.0	0.0
6	0.0	0.0	0.0	0.0	0.0	0.0	0.0	0.0
7	0.0	0.0	0.0	0.0	0.0	0.0	0.0	0.0

$[DEMA]^+$-OH

Contribution%	0	1	2	3	4	5	6	7
0	0.0	100.0	0.0	0.0	0.0	0.0	0.0	0.0
1	0.0	0.0	0.0	0.0	0.0	0.0	0.0	0.0
2	0.0	0.0	0.0	0.0	0.0	0.0	0.0	0.0
3	0.0	0.0	0.0	0.0	0.0	0.0	0.0	0.0
4	0.0	0.0	0.0	0.0	0.0	0.0	0.0	0.0
5	0.0	0.0	0.0	0.0	0.0	0.0	0.0	0.0
6	0.0	0.0	0.0	0.0	0.0	0.0	0.0	0.0
7	0.0	0.0	0.0	0.0	0.0	0.0	0.0	0.0

$[C_4Him]^+$-OH

Contribution%	0	1	2	3	4	5	6	7
0	0.0	100.0	0.0	0.0	0.0	0.0	0.0	0.0
1	0.0	0.0	0.0	0.0	0.0	0.0	0.0	0.0
2	0.0	0.0	0.0	0.0	0.0	0.0	0.0	0.0
3	0.0	0.0	0.0	0.0	0.0	0.0	0.0	0.0
4	0.0	0.0	0.0	0.0	0.0	0.0	0.0	0.0
5	0.0	0.0	0.0	0.0	0.0	0.0	0.0	0.0
6	0.0	0.0	0.0	0.0	0.0	0.0	0.0	0.0
7	0.0	0.0	0.0	0.0	0.0	0.0	0.0	0.0

Supplementary Table 7. Summary of P_{μ}, $S_{\mu,\nu}{}^2$ and activation energies of $[Cation]^+$-OOH in the (0, 0) and (0, 3) state. μ represent the reactant of ORR (oxidized states) and ν represent the product of ORR (reduced states). The activation energies were defined as $\Delta G^{\dagger}_{\mu,\nu} = \frac{(\Delta G^0_{\mu,\nu}+\lambda)^2}{4\lambda}$ (12). The calculation methods were depicted in Supplementary Methods. The contributing state discussed in manuscript are highlighted in table. The P_0S_{03} and P_0S_{00} of two main contributing states of [DEMA]-OOH are both evidently higher than those of two other cations and dominate the increase in overall rate constant.

$[MTBD]^+$-OOH

(μ, ν)	P_{μ}	$S_{\mu,\nu}{}^2$	$P_{\mu}\,S_{\mu,\nu}{}^2$	$\Delta G_{\mu,\nu}{}^{\dagger}$/eV
(0, 0)	1	7.97E-12	7.97E-12	0.243
(0, 3)	**1**	**4.29E-01**	**4.29E-01**	**0.749**

$[DEMA]^+$-OOH

(μ, ν)	P_{μ}	$S_{\mu,\nu}{}^2$	$P_{\mu}\,S_{\mu,\nu}{}^2$	$\Delta G_{\mu,\nu}{}^{\dagger}$/eV
(0, 0)	**1**	**3.89E-09**	**3.89E-09**	**0.294**
(0, 3)	**1**	**8.01E-01**	**8.01E-01**	**0.746**

$[C_4Him]^+$-OOH

(μ, ν)	P_{μ}	$S_{\mu,\nu}{}^2$	$P_{\mu}\,S_{\mu,\nu}{}^2$	$\Delta G_{\mu,\nu}{}^{\dagger}$/eV
(0, 0)	1	4.27E-11	4.27E-11	0.294
(0, 3)	**1**	**4.08E-01**	**4.08E-01**	**0.749**

Supplementary Table 8. Summary of P_μ, $S_{\mu,\nu}{}^2$ and activation energies of $[Cation]^+$-OH in the (1, 0) state. μ represent the reactant of ORR (oxidized states) and ν represent the product of ORR (reduced states). The activation energies were defined as $\Delta G^{\dagger}_{\mu,\nu} = \frac{(\Delta G^{0}_{\mu,\nu}+\lambda)^2}{4\lambda}$ (12). The calculation methods were depicted in Supplementary Methods. (1, 0) is the contributing state, which account for more than 99% in overall rate constant. Therefore, the P_1S_{10} dominate the increase in overall kinetic.

$[MTBD]^+$-OH

(μ, ν)	P_μ	$S_{\mu,\nu}{}^2$	$P_\mu S_{\mu,\nu}{}^2$	$\Delta G_{\mu,\nu}{}^{\dagger}$/eV
(1, 0)	0.01023	0.502982	5.15E-03	0.234

$[DEMA]^+$-OH

(μ, ν)	P_μ	$S_{\mu,\nu}{}^2$	$P_\mu S_{\mu,\nu}{}^2$	$\Delta G_{\mu,\nu}{}^{\dagger}$/eV
(1, 0)	0.000644	0.911987	5.87E-04	0.211

$[C_4Him]^+$-OH

(μ, ν)	P_μ	$S_{\mu,\nu}{}^2$	$P_\mu S_{\mu,\nu}{}^2$	$\Delta G_{\mu,\nu}{}^{\dagger}$/eV
(1, 0)	0.000209	0.980744	2.05E-04	0.196

Supplementary Table 9 Summary of overall kinetic constant and exchange current density of PCET reaction (OOH + H^++e^- = H_2O_2) for $[Cation]^+$-OOH H-bonding species. k_0 is the overall reaction constant, which calculated follow the rate constant expression depicted in Supplementary Methods. The Normalized PCET J_0 (simulated) and Normalized ORR J_0 (Experiment) is obtained via dividing PCET J_0 (simulated) and ORR J_0 (Experiment) of different H-bonding species by PCET J_0 (simulated) and ORR J_0 (Experiment) of $[C_4Him]^+$-OOH. The PCET J_0 is calculated from k_0, following the equation: $J_0 = nFk_0c_\mu$ (13), n is the number of electrons transferred, F is Faraday constant, and c_v is the concentration of ORR intermediate. ORR J_0 (Experiment) is extracted from Butler-Volmer equation, depicting in Supplementary Figure 8.

$[MTBD]^+$-OOH

k_0	Normalized PCET J_0 (Simulated)	Normalized ORR J_0 (Experiment)
2.67E-11	1.09	1.05

$[DEMA]^+$-OOH

k_0	Normalized PCET J_0 (Simulated)	Normalized ORR J_0 (Experiment)
9.94E-11	4.07	2.33

$[C_4Him]^+$-OOH

k_0	Normalized PCET J_0 (Simulated)	Normalized ORR J_0 (Experiment)
2.44E-11	1	1

Supplementary Table 10 Summary of overall kinetic constant and exchange current density of PCET reaction (OH + H^++e^- = H_2O) for [Cation]$^+$-OH H-bonding species. k_0 is the overall reaction constant, which calculated follow the rate constant expression depicted in Supplementary Methods. The Normalized PCET J_0 (simulated) and Normalized ORR J_0 (Experiment) is obtained via dividing PCET J_0 (simulated) and ORR J_0 (Experiment) of different H-bonding species by PCET J_0 (simulated) and ORR J_0 (Experiment) of [C_4Him]$^+$-OH. The PCET J_0 is calculated from k_0, following the equation: $J_0 = nFk_0c_\mu$ (13), n is the number of electrons transferred, F is Faraday constant, and c_v is the concentration of ORR intermediate. ORR J_0 (Experiment) is extracted from Butler-Volmer equation, depicting in Supplementary Figure 9.

[MTBD]$^+$-OH

k_0	Normalized PCET J_0 (Simulated)	Normalized ORR J_0 (Experiment)
1.58E-4	5.88	2.33

[DEMA]$^+$-OH

k_0	Normalized PCET J_0 (Simulated)	Normalized ORR J_0 (Experiment)
4.35E-05	1.62	1.47

[C_4Him]$^+$-OH

k_0	Normalized PCET J_0 (Simulated)	Normalized ORR J_0 (Experiment)
2.69E-05	1	1

Supplementary Table 11 Summary of normalized J_0 of different H-bonding species when the reorganization energy varied (λ=0.75 eV, 1 eV and 1.25 eV).

λ / eV	Normalized PCET J_0 ($[MTBD]^+$-OOH)	Normalized PCET J_0 ($[DEMA]^+$ -OOH)	Normalized PCET J_0 ($[C_4Him]^+$-OOH)
0.75	1	9.45	1
1	1.09	4.07	1
1.25	1.11	3.03	1

λ / eV	Normalized PCET J_0 ($[MTBD]^+$-OH)	Normalized PCET J_0 ($[DEMA]^+$ -OH)	Normalized PCET J_0 ($[C_4Him]^+$ -OH)
0.75	6.39	1.68	1
1	5.88	1.62	1
1.25	5.60	1.58	1

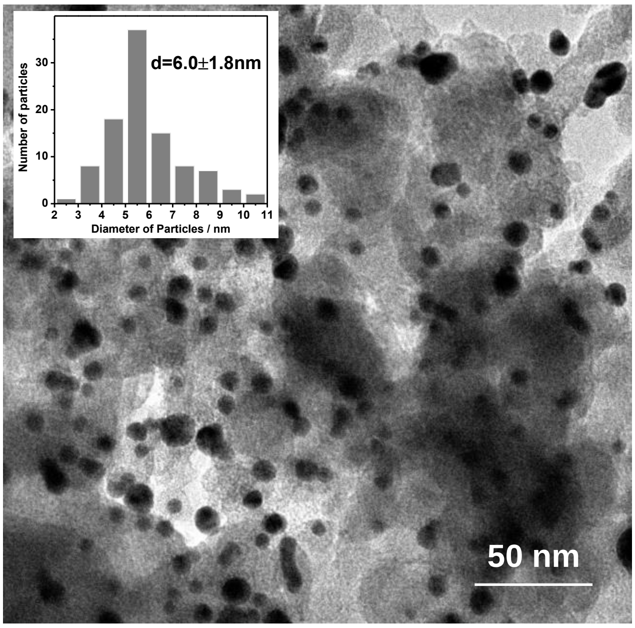

Supplementary Figure 29: The TEM pictures of Au/C nanoparticles, the Au loading is 30%.

Supplementary References

1. Bard AJ, Faulkner LR, Leddy J, Zoski CG. Electrochemical methods: fundamentals and applications, vol. 2. Wiley New York, 1980.

2. Lu Y-C, Gasteiger HA, Shao-Horn Y. Catalytic activity trends of oxygen reduction reaction for nonaqueous Li-air batteries. *J. Am. Chem. Soc.* **133**, 19048-19051 (2011).

3. Zeng Y, Smith RB, Bai P, Bazant MZ. Simple formula for Marcus–Hush–Chidsey kinetics. *J. Electroanal. Chem.* **735**, 77-83 (2014).

4. Bai P, Bazant MZ. Charge transfer kinetics at the solid-solid interface in porous electrodes. *Nat. Commun.* **5**, 3585 (2014).

5. Horvath S, Fernandez LE, Soudackov AV, Hammes-Schiffer S. Insights into proton-coupled electron transfer mechanisms of electrocatalytic H2 oxidation and production. *Proc. Natl. Acad. Sci. U. S. A.* **109**, 15663-15668 (2012).

6. Frisch M, Trucks G, Schlegel H, Scuseria G, Robb M, Cheeseman J, *et al.* Gaussian 09, Revision D. 01; Gaussian: Wallingford, CT, (2009).

7. Laury ML, Carlson MJ, Wilson AK. Vibrational frequency scale factors for density functional theory and the polarization consistent basis sets. *J. Comput. Chem.* **33**, 2380-2387 (2012).

8. Webb SP, Hammes-Schiffer S. Fourier grid Hamiltonian multiconfigurational self-consistent-field: A method to calculate multidimensional hydrogen vibrational wavefunctions. *J. Chem. Phys.* **113**, 5214-5227 (2000).

9. Hammes-Schiffer S. webPCET Application Server. http://webpcet.chem.yale.edu: Yale University; 2009.

10. Hammes-Schiffer S, Soudackov AV. Proton-coupled electron transfer in solution, proteins, and electrochemistry. *J. Phys. Chem. B* **112**, 14108-14123 (2008).

11. Costentin C, Evans DH, Robert M, Savéant J-M, Singh PS. Electrochemical approach to concerted proton and electron transfers. Reduction of the water− superoxide ion complex. *J. Am. Chem. Soc.* **127**, 12490-12491 (2005).

12. Weingärtner H. The static dielectric permittivity of ionic liquids. *J. Mol. Liq.* **192**, 185-190 (2014).

13. Wakai C, Oleinikova A, Ott M, Weingärtner H. How polar are ionic liquids? Determination of the static dielectric constant of an imidazolium-based ionic liquid by microwave dielectric spectroscopy. *J. Phys. Chem. B* **109**, 17028-17030 (2005).

14. Koper MTM. Volcano Activity Relationships for Proton-Coupled Electron Transfer Reactions in Electrocatalysis. *Top. Catal*. **58**, 1153-1158 (2015).

15. Koper MT. Theory of the transition from sequential to concerted electrochemical proton-electron transfer. *Phys. Chem. Chem. Phys.* **15**, 1399-1407 (2013).

16. Ford DC, Nilekar AU, Xu Y, Mavrikakis M. Partial and complete reduction of O2 by hydrogen on transition metal surfaces. *Surf. Sci.* **604**, 1565-1575 (2010).

17. Koper MT. Theory of multiple proton–electron transfer reactions and its implications for electrocatalysis. *Chem. Sci*. **4**, 2710-2723 (2013).

18. Chevalet J, Rouelle F, Gierst L, Lambert JP. Electrogeneration and some properties of the superoxide ion in aqueous solutions. *J. Electroanal. Chem. Interf. Electrochem.* **39**, 201-216 (1972).

19. Costentin C, Evans DH, Robert M, Saveant JM, Singh PS. Electrochemical approach to concerted proton and electron transfers. Reduction of the water-superoxide ion complex. *J. Am. Chem. Soc.* **127**, 12490-12491 (2005).

20. Casalongue HS, Kaya S, Viswanathan V, Miller DJ, Friebel D, Hansen HA, *et al.* Direct observation of the oxygenated species during oxygen reduction on a platinum fuel cell cathode. *Nat. Commun.* **4**, (2013).

21. Wakisaka M, Suzuki H, Mitsui S, Uchida H, Watanabe M. Increased Oxygen Coverage at Pt−Fe Alloy Cathode for the Enhanced Oxygen Reduction Reaction Studied by EC−XPS. *J. Phys. Chem. C* **112**, 2750-2755 (2008).

22. Wakai C, Oleinikova A, Ott M, Weingartner H. How polar are ionic liquids? Determination of the static dielectric constant of an imidazolium-based ionic liquid by microwave dielectric spectroscopy. *J. Phys. Chem. B* **109**, 17028-17030 (2005).

23. Uematsu M, Frank EU. Static Dielectric Constant of Water and Steam. *J. Phys. Chem. Ref. Data* **9**, 1291-1306 (1980).

24. Quaino P, Luque NB, Nazmutdinov R, Santos E, Schmickler W. Why is gold such a good catalyst for oxygen reduction in alkaline media? *Angew. Chem. Int. Ed.* **51**, 12997-13000 (2012).

25. Bolton JR, Archer MD. Basic Electron-Transfer Theory In Electron Transfer in Inorganic, Organic, and Biological Systems, in *Advances in Chemistry*, vol. 228, American Chemical Society, 1991, 7-23.

26. Newton MD, Sutin N. Electron Transfer Reactions in Condensed Phases. *Annu. Rev. Phys. Chem.* **35**, 437-480 (1984).